August 2021

Exploiting Multi Stability of Compliant Locking Mechanism for Reconfigurable Articulation in Robotic Arm

Troy Justin Carhart
Clemson University, tcarhart@yahoo.com

EXPLOITING MULTI STABILITY OF COMPLIANT LOCKING MECHANISM FOR RECONFIGURABLE ARTICULATION IN ROBOTIC ARM

A Thesis
Presented to
the Graduate School of
Clemson University

In Partial Fulfillment
of the Requirements for the Degree
Master of Science
Mechanical Engineering

---

by
Troy Justin Carhart
August 2021

Accepted by:
Dr. Suyi Li, Committee Chair
Dr. Oliver Myers
Dr. Ian Walker

ABSTRACT

This study analyzes a biology inspired approach of utilizing a compliant unit actuator to simplify the control requirements for a soft robotic arm. A robot arm is constructed from a series of compliant unit actuators that precisely actuate between two stable states. The extended state can be characterized as a rigid link with a high bending stiffness. The compressed state can be characterized as a flexible joint with a low bending stiffness. Without the use of an external power source, the bistable mechanism remains in each of the stable states. The unit actuator can demonstrate pseudo-linkage kinematics that require less control parameters than entirely soft manipulators. An advantage of using compliant mechanisms to design a robotic arm is that the bending stiffness ratio between the extended and compressed states is related to the frame and flexural member geometry. Post buckling characteristics of thin flexural members, combined with a cantilever style frame design gives the unit actuator versatile advantages over existing actuator designs like layer jamming and shape memory polymers. To achieve efficient movement with the optimized unit actuator design, experimental validation was performed, and a robotic arm prototype was fabricated. The tendon-driven robotic arm consisted of three modules and proved the capability of transforming and rotating in the eight configurations. The deformations of the robotic arm are accurately predicted by the kinematic model and validate the compliant mechanism arm and simple control system.

Keywords: Compliant Mechanism, Multi-Stability, Articulation, Robotic Arm

DEDICATION

I dedicate my thesis work to my family and many colleagues that have helped me in my ongoing professional achievements. A special feeling a gratitude to my loving wife, Emily Carhart who has never left my side and encouraged me in every step I have taken as an engineer. My parents Scott and Judy Carhart, who have always encouraged and supported me no matter how high I set my goals.

I also dedicate this thesis to my many classmates and professors at Anderson University and Clemson University who have instilled a passion for education in me. I will always appreciate the roles they played in my education, especially Dr. Charles Raines for showing me that physics surrounds our everyday life and Dr. Suyi Li for supporting my growth as a student and researcher in dynamic matter.

I dedicate this work and give the ultimate thanks to God. He created me and gave me a passion for engineering and education. Throughout my past, present, and future works, may my career glorify God and God alone.

ACKNOWLEDGEMENTS

I wish to thank my committee members who willingly gave their precious time and expertise. A special thanks to Dr. Suyi Li, my committee chair for all the meetings, research discussions, and lab resources. Without his leadership and guidance, I would not have been able to make the academic achievements I have made. Thank you, Dr. Oliver Myers, and Dr. Ian Walker, for agreeing to be members of my thesis committee.

I would like to acknowledge and thank Clemson University for granting me the opportunity to advance academically, perform research, and accept accepting the university's help over the entire process. Thank you to the Mechanical Engineering department for developing me into a well-rounded Mechanical Engineer. A special thanks to my lab mates in the Dynamic Matter Group for accepting me as a member of the lab and supporting my research.

Finally, I would like to thank all the teachers, mentors, and administrators from the schools I have attended. Their enthusiasm and constructive feedback have challenged me to set high academic goals and pursue a lifetime of learning.

TABLE OF CONTENTS

Page

Table of Contents (Continued)

Page

Table of Contents (Continued)

Page

LIST OF TABLES

LIST OF FIGURES

List of Figures (Continued)

List of Figures (Continued)

CHAPTER ONE

INTRODUCTION

Research Motivation

The ongoing advances in biomimicry, material science, fabrication technology, and control theory are enabling engineers to develop soft robots (robotic manipulators) that can work with humans in unstructured and changing environments [1-3]. Soft robots can adapt and passively deform around objects in its working environment. Elastic material allows mechanisms to achieve soft robotic characteristics. Material is chosen based on its low elastic moduli and high strain rates before failure, properties that keep mechanisms strong and flexible [4]. Flexible linkages are safer for human robot interaction because they pose less of a threat to sensitive working environments like surgical operating rooms [5-6]. Traditional rigid link robots can produce sharp pinch points, disturb sensitive object in the surroundings, and get stuck in an unpredictable environment. Soft robotics is bridging a gap that brings smart structures and adaptability to tradition robotics [7].

Implementing compliance in robotic arms designs pose challenges in the control and modeling process [8]. Many scientists seek soft robotic innovation by looking towards nature. Nature is full of flexible bodies and reconfigurable structures that are made of soft skins, elastic muscles, and flexible tendons. Each new material that is implemented into a soft structure further complicates the controls process by introducing underlying material properties [9]. The neural networks in biological systems

continuously adapt and learn to fully utilize the complex systems in an organism. In designing soft robots, scientists need to design preprogrammed motion patterns for artificial systems that are inspired by natural autonomous systems that constantly adapt. Nonlinear mechanics make it complicated to predict pinpoint movement in sensitive and unstable environments and complex control architecture needs to reflect complex dynamics that are affected by changing material properties. Elastic robotic bodies can introduce viscoelastic material properties that increase uncertainty and predictability in a system. The field of soft robotics is far from safe controllable commercial use. The possibilities of soft robotics make the future research and development of soft robotic systems and simplified control techniques worth pursuing.

The most common approach to combating soft robotic challenges is to reduce the degrees of freedom in a structure to increase controllability [10]. Nature supplies us with ample examples of compliant structures that utilize this strategy. For example, the octopus achieves pinpoint movements of its arm when hunting for prey. Figure 1.1 shows an octopus extending its arm to snatch its prey and then compressing is back so it can secure the prey. All this is done in 0.82 seconds. Rather than focusing on a specific end effector design, researchers have been drawing inspiration of the octopus's ability to adjust the length and position of each of its arm segments to deploy to a specific location in space and wrap around a desired object. This quasi-articulated arms structure is achieved by controlling the stiffness of each segment throughout the entire arm. The

process of stiffening and relaxing individual arm segments allows the octopus to transform an arm of infinite degrees of freedom, to an arm of controllable degrees of freedom [1]. Each arm segment when stiffened acts as a rigid link; when the segment is relaxed, the arm segment acts as a soft joint capable of rotational movement. Through this process, the octopus controls its arm that compresses, elongates, and rotates on demand.

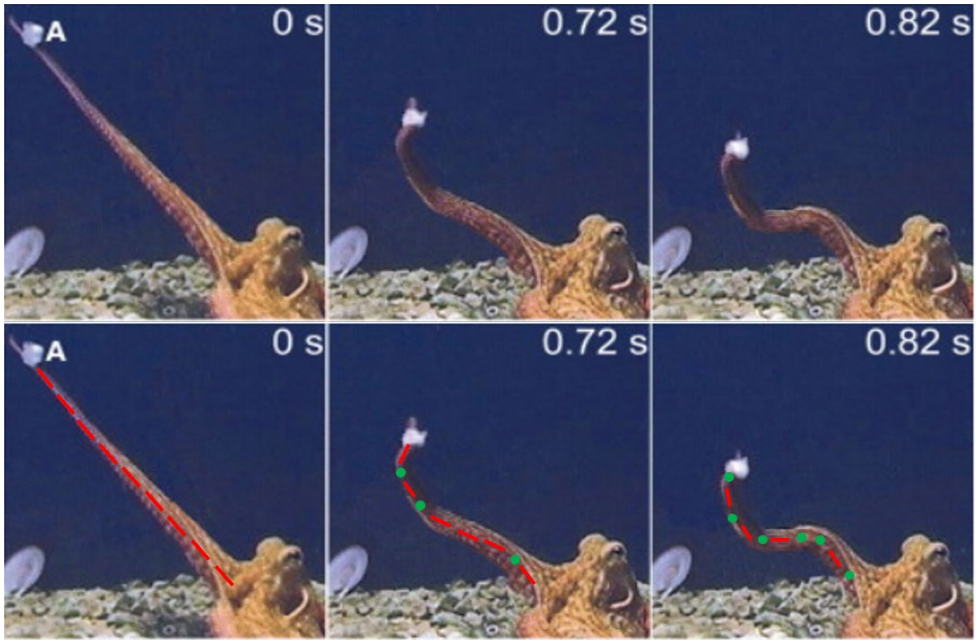

Figure 1.1: An octopus controlling the stiffness of its arm to catch its prey. Red lines show rigid links and green dots show flexible joints. [12].

There have been four major attempts to explore the bioinspired robotic arm design with tunable stiffness. Layer jamming is a technique that uses overlapping flexible flaps to control the stiffness of a robotic arm segment [13-14]. The more flaps in an individual

segment that overlap, the higher the bending stiffness will be. The bending stiffness is controlled by overlapping flaps create a larger contact surface that increases the internal friction of the segment. These layers are controlled through vacuum-pressure; when a specific pressure is applied, the unique interactions between the layers change the mechanical properties of the systems. This process requires special pumps to control the actuation and precise sensors to detect changing pressures, causing the fabrication of such arm to be complex.

Another design utilizes low melting point materials to manipulate robotic arm segments. A solder-based locking joint was used to create a small-scale series of segments. When the solder is below the melting point, the joint is rigid. A resistive heating element was designed into the arm to raise the temperature above the melting point, transforming the rigid link into a flexible joint [15]. The third design was fabricated with a shape memory polymer joint. In the robotic arm joint, a heater is used to transition a thin polymer link into a folded state. This allows the robotic arm to change the stiffness of each segment to form unique configurations [16]. These three methods of fabricating soft robotic arms show feasibility, but introduce problems in complex construction, difficult kinematics, and continuous energy to transition and maintain changes in stiffness.

A more recent attempt of harnessing continuous soft robotic arm capabilities used Kresling origami structures. Each Kresling unit exhibited predictable bistability that

switched the unit from a soft state of low bending stiffness to a rigid state with a high bending stiffness. Here, the serially connected links remained in their preset stable states without an external continuous power supply [1]. The prototype robotic arm proved the functionality of a tendon-driven robotic and posed a suitable analytical prediction model for the bistable mechanism. However, the arm suffered from instability when acted upon by disturbance forces, causing individual units to make unwanted transitions from their desired stable states. The reconfigurable robotic arm reduced control efforts but created the need for a lockable unit structure.

To achieve localized stiffness tuning for soft robotics in a modular and energy-passive manner, we look to analyze and develop the bistable mechanics of a compliant unit actuator mechanism. Compliant mechanisms are designed around deflections of thin flexural members and are fabricated as one-piece plastic frames. This reduces the part counts of a mechanism and further simplifies the fabrication process with 3D printing. Bistability can be achieved by inducing deflections upon the thin links that are accurately controlled by rigidity of thicker frame dimensions. Introducing bistability to a soft robotic design will reduce the energy consumption when at rest. By serially connecting bistable compliant actuators, the degrees of freedom can be controlled; and a binary control method can be used to reduce the complexity of controlling the kinematics. The stable states create joints and links at desired locations about the robotic arm. This soft robotic design approach is unique because the stiffness tuning each unit mechanism is controlled

by the material properties and geometric properties of the frame, making the compliant actuators easily scalable for different tasks. Overall, compliant mechanisms will solve the complex problems in soft manipulators by reducing part counts with additive manufacturing, simplifying control methods with lockable equilibrium positions, and reducing energy consumption with bistability.

Research Scope and Purpose

Constructing a robotic arm using compliant unit actuators is a complex and multistep task. Robotic arms require high accuracy motion sensing, automated actuation, closed-loop controls, and precision designs and fabrication. This thesis will focus on two major aspects of the robotic arm: the design and validation of a compliant unit actuator and the construction of a proof-of-concept robotic arm system capable of controlled articulations. The objectives of the finalized design are as followed:

1. The compliant unit actuator must have a robust difference in bending stiffness between the two stable states. A significant difference in the bending stiffness of the stable states is key to performing soft robotic articulations.
2. The compliant unit actuator must serially connect. The number of connected unit actuators can change based on the task of the robotic arm. Having series connection allows the robotic arm to be modular and adapt to the needs of an end user's tasks.

3. The compliant unit actuator must maximize the stroke between the two stable states. Deployable structures are more useful with an increased range of motion [17].
4. The robotic arm must articulate in an extendable, compressible, and rotatable fashion. Extensions, compressions, and rotation allow the robotic arm to operate in a single 2D planar frame.
5. The robotic arm must not be affected by external load disturbances. In a 2D plane, the robotic arm can be subject to compression, tensile, and moment loads. While controlled loads will cause the robotic arm to reconfigure, disturbance loads should not break the configurations or predicted movements of the robotic arm.
6. The compliant unit actuator must be lockable in the rigid link state and unlock before transitioning to the soft joint state. Locking the rigid link state builds upon the advances made in the Kresling origami method.
7. The robotic arm must be controllable in all configurations. The deformation of the robotic arm must be consistent with a kinematic model to prove feasibility.

Thesis Outline

We begin by researching background information for compliant mechanisms, bistability, and robotic arm articulation in chapter 2. Chapter 3 consists of the part design of a compliant unit actuator including the frame, locking mechanism, flexural members, and spine. Next, chapter 4 will detail the fabrication and assembly of the unit actuator.

Chapter 5 will layout the testing plans and results for the bending stiffness test, cycle test, and unlocking test. Chapter 6 will detail the robotic arm design and the control method. Chapter 7 will layout the testing plan and results robotic arm configurations test and the controls test. Chapter 8 will conclude the research project and introduce future research opportunities.

CHAPTER TWO

BACKGROUND RESEARCH

Variable stiffness actuators (VSAs) use elastic components to change the stiffness of a mechanism, usually between a rigid link of high bending stiffness, and a soft joint of low bending stiffness [18]. Differing the stiffness allows the actuator to control its degrees of freedom. Instead of simply translating back-and-forth in a longitudinal direction, actuators can be designed to rotate as well [19]. Rotational elements are designed into the soft state of the mechanism and make the VSA safer. A variable stiffness actuator needs to meet five key design features:

1. A robust stiffness ratio that allows the mechanism to exhibit precision tasks in a completely rigid, high stiffness state and allow for safe interactions in a soft, low stiffness state.
2. A functional deflection range that can handle minor disturbances like impacts and vibration.
3. A compact design that allows the mechanism to be used in small areas yet extended to provide significant reach.
4. A low energy consumption to maintain stiffness states, best accomplished through bistability.
5. A reproduceable design that makes for an easy manufacturing process.

Based on these five design elements, research into related topics drive this research thesis. The following subsections: compliant mechanisms, stability, slender beams, and robot arm articulation, will review the topics that played a major role in the development of the multi-stable, locking compliant mechanism used for a robotic arm.

Compliant Mechanisms

Compliant mechanisms are structures that transfers load, movements, or energy through flexible components. Traditional mechanisms are designed with rigid links and joints that each accomplish a specific task in the machine. A spring and a hinge are examples of mechanical components that are commonly incorporated into traditional mechanism. Compliant mechanisms are designed to reduce part counts by assigning multiple tasks to an individual component [5, 20]. This allows compliant mechanisms to be efficient at accomplishing an overall task, but it increases the difficulty of designing such a mechanism.

Nature fuels the creative design of compliant mechanisms. Figure 2.1 displays examples of natural and man-made compliant mechanisms. The figures on the left show an earth worm and an octopus. The earthworm is comprised of many soft joints that keep its entire structure flexible while transferring loads, movement, and energy through its body. The octopus arm contains the same design elements as the worm and can deploys its arm to pinpoint locations to snatch prey. An octopus can stiffen and relax the individual segments that make up its arm. The stiffened segments act like rigid links and

the relaxed segments act like joint. By controlling the sequence of stiffened and relaxed arm segments, the octopus controls the degrees of freedom in its arm and deploys it with pinpoint accuracy.

The photos on the right show two man-made compliant mechanisms: a bow and a gripper. Ancient hunters used thin wooden sections carves into wooden bows to create a flexible segment in the weapon. The spring like effect allowed warriors to pull back on a piece of string, create a deflection in the thin section of the bow, store the energy as they held the string back, and finally release the string and send an arrow speeding through the air. The gripper is a modern example of a compliant mechanism. It mimics the design of a set of vice grips. Instead of the pinned joints and springs in traditional vice grips, this design uses thin flexural members to create displacements with the deflection energy. Unlike the vice grips, this compliant gripper is made of a single piece of 3D printed polymer and creates the same force amplification as the vice grips.

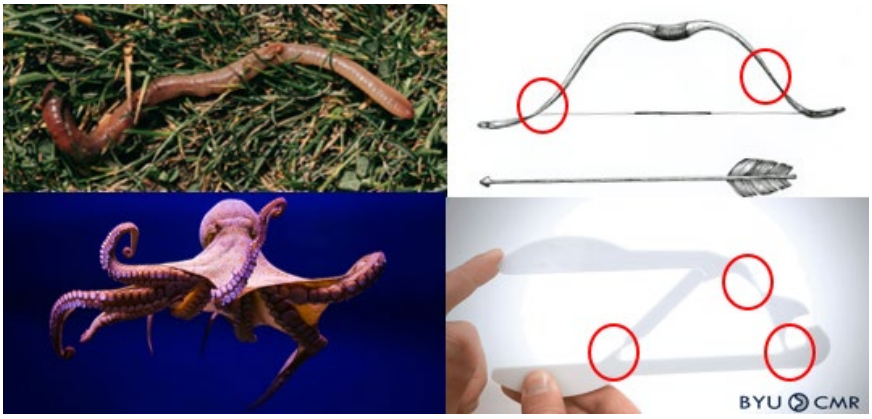

Figure 2.1: Examples of natural and man-made compliant mechanisms. The left section of the figure shows the flexible body structure of a common earthworm and an octopus. The right section of the figure shows an ancient bow design used throughout history and a modern gripper mechanism used to replace a tradition set of vice grips [5].

Compliant mechanisms offer high precision movement, low manufacturing cost, and a large scalable size range. Two main concepts are fundamental to understand for compliant mechanisms. First, stiffness is not the same as strength [5]. Many traditional structures are stiff and strong. Strength is the resistance to failure and stiffness is the resistance to deflection. Second, mechanisms can be designed to be strong and flexible. This is done by decreasing the stiffness of a structure and keeping the strength high. This is a complicated process and requires an engineer to design around material properties, geometry of a structure, and boundary loading conditions.

Stability

A system experiences stability when it remains in a position without the input of an external force. At a stable position, a mechanism will return to that position when

exposed to a disturbance force. A bistable mechanism contains two stable equilibrium points within its range of motion. The transition between stable positions can be initiated through a tensile or compressive force acting upon the mechanism. If the force reaches a critical value, the mechanism will transition into an unstable state and snap through to the other stable state. Figure 2.2 displays a ball on a hill analogy used to explain stable positions and degrees of stability.

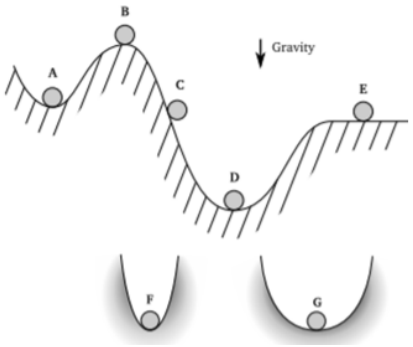

Figure 2.2: Visual ball-on-a-hill analogy used to explain the potential energy stability equilibrium and a valley analogy used to explain the degree of stability [21]

Positions A and D show stable equilibrium 1 and 2. From these positions, the ball can be forced to displace up the hill and still return to the original position. Position B shows the unstable equilibrium. An input for from either direction will push the ball down the hill and into another position. Position C is visually showing a ball transitioning from the equilibrium A to the stable equilibrium D. The C ball must be moved up to the unstable equilibrium B with a critical force before can transition to the next stable equilibrium. The vertical distance between A and B, also D and B represent the critical value needed to make

the ball snap through positions. Position E displays neutral stability. Given an input force from either direction, the ball will roll out of the position, but remain on the stable level. Positions F and G visually the degrees of stability by changing the curvature of the valley. Position F is a more stable position because the curvature is steeper compared to the valley at position G. Figure 2.3 shows the graphical representation of stability through force, energy, and stiffness curves.

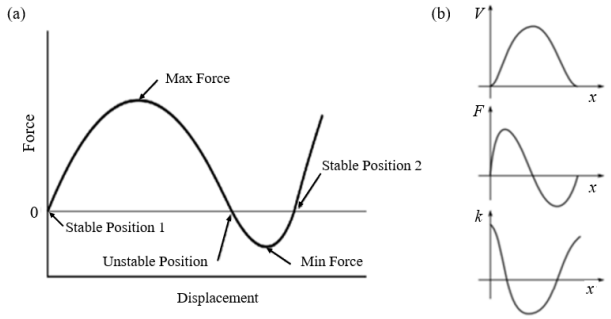

Figure 2.3: Bistable mechanism graphs: (a) Critical points of a force-displacement curve (b) potential energy curve V, force-displacement curve F, and stiffness curve k. [22-23]

The input force is the force required to produce a specific deformation of the compliant mechanism. Stability is defined as the position that requires zero input force to keep the system in the equilibrium position. Two types of stability are displayed in figure 2.3a: positive and negative. A position of positive stability, such as stable position 1 and 2, will remain in the equilibrium position when it is exposed to a small external force. The stroke of a bistable mechanism is calculated using the equation:

$$\Delta x = x_2 - x_1 \tag{2.1}$$

where Δx is the stroke, x_2 is the second stable position and x_1 is the first stable position. The stable equilibrium positions have positive stiffness and are located at the same displacement position as the maximum position on the stiffness graph k.

A position of negative stability will come out of an equilibrium position when exposed to a small external force. This is the unstable equilibrium position. The unstable equilibrium position has a negative stiffness and is located at the same displacement position as the minimum on the stiffness graph k [23]. The critical force is the force required to transition a system from one stable equilibrium to another; for compliant mechanisms this is known as the snap through process [snap through]. The maximum input force must be larger than the critical force to switch equilibrium positions. Figure 2.3b shows that the two critical forces, the maximum force, and the minimum force, are at the displacement positions as the zero on the stiffness curve k. Looking at the V curve in figure 2.3b, the area under the curve is equal to the total energy needed to transition a system from one stable equilibrium position to another.

Slender Beam Buckling

Structures supported by a thin, slender beam can be subject to buckling under a critical value. Typically, engineers design structures to resist buckling. Designing a structure around buckling is useful within bistable mechanisms because of the post buckling characteristics [24]. Buckling a beam is based on the structural dimensions of

the of the beam and the load exerted on the beams. Euler stated that the critical buckling value is determined by the equation:

$$P_{cr} = \frac{C\pi^2 EA}{(L/r)^2} \tag{2.2}$$

where P_{cr} is the critical buckling load, E is the modulus of elasticity of the column material, A is the cross-sectional area of the column, L is the unsupported length of the column, and C is the column effective length factor. It will be assumed that the end conditions for this thesis are fixed-fixed, giving a theoretical C value of 4 and a recommended design C value of 1.2 [25-26].

In structural engineering, beams are considered slender or short to determine their failure modes. Short beams fail due to crushing and slender beams fail due to buckling. A beam can be classified as short or slender based on its slenderness ratio [27]. Bistable mechanisms need to utilize slender column buckling instead of crushing to minimize the plastic deformation within the column material. The slenderness ratio equation is:

$$\lambda = \frac{L}{r} \tag{2.3}$$

where λ is the slenderness ratio and r is the least radius of gyration. The radius of gyration is calculated using the equation:

$$r = \sqrt{\frac{I}{A}} \tag{2.4}$$

where I is the area moment of inertia. When the slenderness ratio of a beam exceeds 100, it can be predicted to fail from buckling and is classified as a slender beam [28]. A structural example of this phenomenon is Figure 2.4 where a mass is supported by two inclined beams.

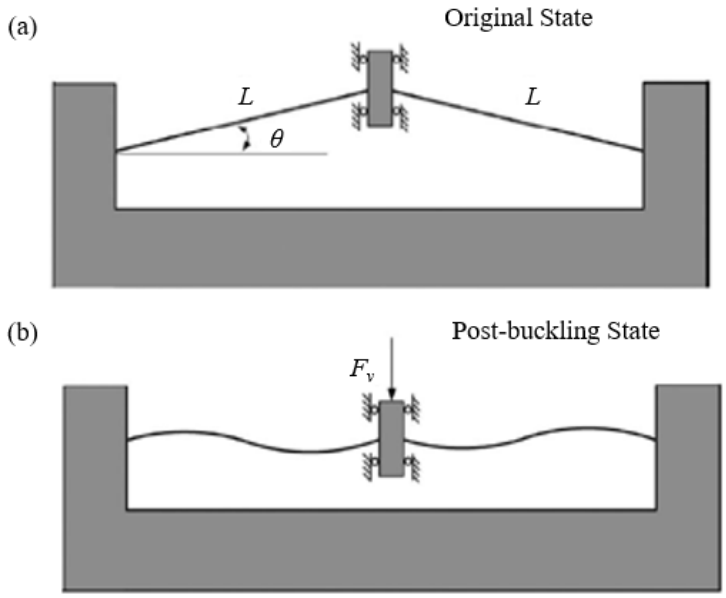

Figure 2.4: A bent beam structure: (a) A slider mass is supported by two inclined slender beams. (b) A critical force induces a buckling failure for the two slender beams, sliding the mass into a post-buckled state [29].

Figure 2.4a shows the slender beams supporting the mass and constraining the vertical movement of the mass. When a load is applied to the mass, the beams will experience compression. Assuming the symmetry of the structure, each beam will experience equivalent force. The vertical force can be increased until it reaches a critical value that will buckle the inclined beams. It is assumed that the outer ends of the column

are fixed ends, and the mass is treated as a slider. The critical buckling force will cause the mass to experience a snap through process that displaces the mass in a linear path and changes the stiffness of the structure, as shown in figure 2.4b. Frames can be designed to hold a central mass in a post-buckled configuration. In this position, the post buckling behavior presents the capability of soft joint like behavior including rotational displacement. When a compliant frame is incorporated with the slender beams, it creates a bistable system. To transition the mass out of the post-buckled position, a vertical force must be applied causing the beams to experience tension. When the tension reaches a critical value, the mass will snap back to the original state and resist longitudinal and rotational displacements.

Robotic Arm Articulation

Rigid link robotic arm articulation can be modeled by the classic Denavit-Hartenberg frame kinematics. A continuous soft robotic arm does not follow the same kinematics; in fact, predicting the end effector position on a soft robotic arm is complicated. Through localized stiffness tuning, a robotic arm can make the transition from a completely rigid structure to an intermediate structure to a completely soft structure. Figure 2.5 displays an overview of the envisioned robotic arm articulation [1]. We can construct a soft robotic arm by serially connecting compliant unit actuator modules that create soft joints and rigid links at desired positions by switching between the two stable states. Figure 2.5b shows how bistability and post-buckling characteristic

of slender beams can be used to reconfigure a robotic arm. The mechanism will remain rigid in an extended stable position and become soft when it is compressed to the compressed stable position. The unique bistability of the unit actuator supports a method of binary bending stiffness tuning seen in figure 2.5c.

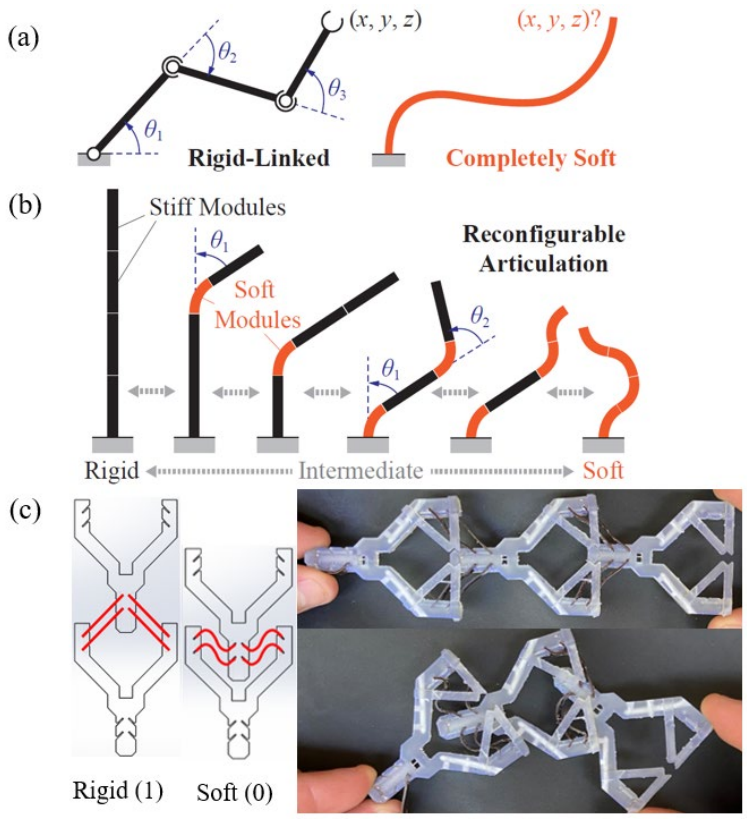

Figure 2.5: A continuous compliant robotic arm articulation method that supports multiple configurations. a) The modern model of a completely rigid and completely soft robotic arm. b) A four-module robotic arm showing multiple articulations. Each module has a stiffness rigid stable state and soft stable state, making the robot capable of being completely rigid (left) and completely soft (right). The robot arm concept has 16 (2^4) unique configurations.[1] c) The compliant unit actuator used in this study showing the desired switch between a soft, low bending stiffness and a rigid, high bending stiffness.

The following design, testing, and results of this study will lay down the groundwork for constructing a new hybrid robotic arm with accurately controlled movement and flexible capabilities.

CHAPTER THREE

COMPLIANT UNIT ACTUATOR DESIGN

The compliant mechanism unit actuator is divided into two major components designed for this research: the frame and the flexural members. The following subsections will discuss the importance and design decisions made for each of the components of the mechanism. Critical dimensions will be identified for each component of the frame. Material and assembly considerations will follow in the fabrication chapter. It is important to note that the frame is not bistable on its own, neither are the flexural members. When the frame is linked to the flexural members, the combined system becomes bistable because of the mechanical performance of the frame and the post buckling characteristics of the thin flexural members.

Frame

The frame is setup as a planar mechanism, motion is intended for longitudinal extension and compression along the y axis and rotation about the z axis. The frame is symmetric about the y axis. A layered approach was used when designing the features of the frame and can be seen in figure 3.1. Three layers are stacked on the z axis: the bottom layer is designed for the robotic arm spine control, the middle layer is the main frame, and the top layer is the locking layer. Dimensional drawings of the frame are in Appendix A. Figure 3.1 displays a labeled diagram of the frame.

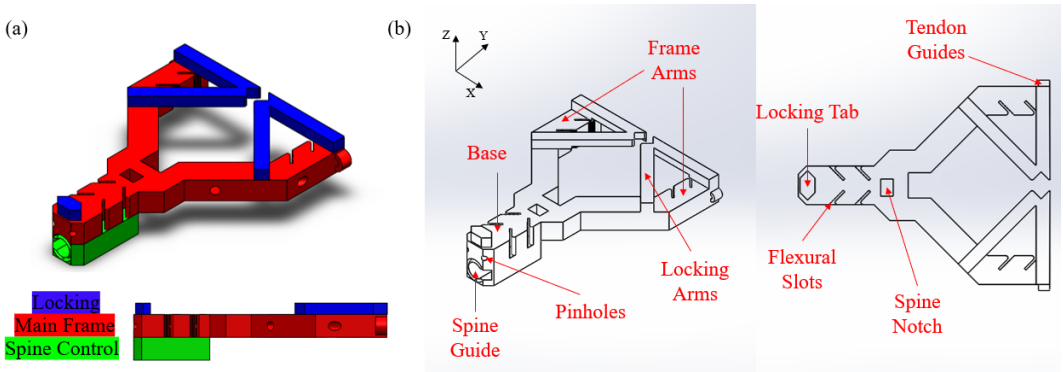

Figure 3.1: A labeled 3D model of the unit actuator frame. a) Labeled layers of the actuator frame: blue is the locking layer, red is the main frame layer, and green is the spine control layer. b) Labeled components of the actuator frame.

Starting with the bottom layer, the spine guide is where the spine for the robotic arm travels through the frame and controls the extension and compression modes. The guided hole is chamfered at the entrance to make the spine insertion easier. The spine guide has a main cylindrical shape for the rod-like body of the spine and a rectangular cut out for the integrated spine tab that locks into the spine notch. This layer is 5mm thick because of the radial dimension of the spine. Further explanation of the spine operations is detailed in following sections of the robotic arm.

The 5mm thick middle layer is the main layer of the frame made up of the base and frame arms. The base consists of the flexural slots and pinholes for fabrication. The flexural slots are designed to be 0.05mm thinner than the flexural members. Along with the integrated assembly pins, the flexural slots will keep the flexural members secured with a press-fit assembly that prevents slipping during the extension and compression cycles. The flexural slots contain an inner knurling pattern. In the event of creep, the

plastic flexural member will slowly deform into the knurling of the frame to create a secure mate between the frame and the flexural member. The angle of the flexural slots is 45 degrees with reference to the y axis. The frame shape was inspired by multi-material deployable structure designed by a research lab in Switzerland [30]. The design used a multi-material 3D printed mechanism to perform motion as a linear actuator. The researchers determined that a 45-degree angle is an efficient angle for actuator performance [30]. An angle smaller than 45 degrees would increase the stroke, increase the resistance to a vertical (y axis) disturbance force, but decrease the resistance to a horizontal (x axis) disturbance force. An angle larger than 45 degrees would increase the resistance to a horizontal disturbance force but decrease the resistance to a vertical force and decrease the stroke.

The frame arms consist of flexural slots, pinholes, and tendon guides. The tendon guide is a small hole where the robotic arm tendons are threaded through for rotational control. Further explanation of the tendons is described in following robotic arm sections. The frame arms take the shape of symmetric cantilever beams. Upon a vertical force, the flexural members will apply a force to the end of the arms and cause them to deflect. Once the critical buckling load of the flexural members has been reached, the frame arms will return to an undeflected position that pushes the buckled flexural members into the compressed position. The arms act like cantilever beams that are fixed at one end of the base, and free at the opposite end. The arms also act like cantilever beams that are loaded

at the free end. The following equation was used to determine the dimensions of the frame arm:

$$M_{max} = FL \tag{3.1}$$

where M_{max} is the max moment at the end of the beam, F is the max horizontal (x axis) force of the beam, and L is the length of the beam. This equation is used to solve for the max deflection equation:

$$\partial_{max} = \frac{FL^3}{3EI} \tag{3.2}$$

where E is the elastic modulus of the beam material, and I is the area moment of inertia of the beam. Eighty seven percent of the of the arm deflection comes from the 45-degree section of the arms. This conclusion was made based on calculations found in Appendix B. In the beam deflection equation, the most significant geometric property is the length of the beam, which magnifies changes to the third power. Also, according to the moment of inertia equation, small changes to frame arm width magnifies the change to the third power. These two dimensions were analyzed as critical design dimensions for testing. The width of the frame arm that allows for ideal end deflection is 6mm.

The top layer of the mechanism is the locking layer and consists of the locking tab and the locking arms. Locking features of the mechanism serve two purposes. In the extended (1) position, the actuator can be locked in a rigid state. When the locking arm

notch is combined with the locking tab, they serve as a defense against moment and force disturbances. The shape of the locking tab is identical to the cut-out notch in the locking arms. Key design dimensions of the features are the notch angle and shape, the notch width, and the locking arm angles.

The locking arms consist of a 90-degree beam and a 45-degree beam. As the frame arms deflect, the locking arms will deflect too, causing the locking arms to release the locking notch from the locking bars. Once unlocked, the mechanism transition from an unstable state to the stable compressed state. The 90-degree beam defends against horizontal and moment loads. When the actuator experiences a moment, the locking tab will distribute the force from the end of the actuator to the 90-degree beam and distribute it about that side of the frame arm. The same concepts applied to horizontal force. The 45-degree beam defends against vertical forces. When the actuator experiences a vertical force, it will be transferred from the locking notch to the 45-degree arms and distributed through the that side of the frame. Decreasing the angle of this beam would allow the actuator to resist larger vertical loads but cause the beam to be attached to a lower section on the frame arm. Bringing the connection point of the locking arm closer to the base of the frame arm would decrease the deflection range because it shortens the lever length of the locking arm as it distributes force to the frame arm. This deflection range is critical when unlocking the notch from the locking arms. This decreased deflection would

increase the locking force to value that makes locking and unlocking the mechanism difficult.

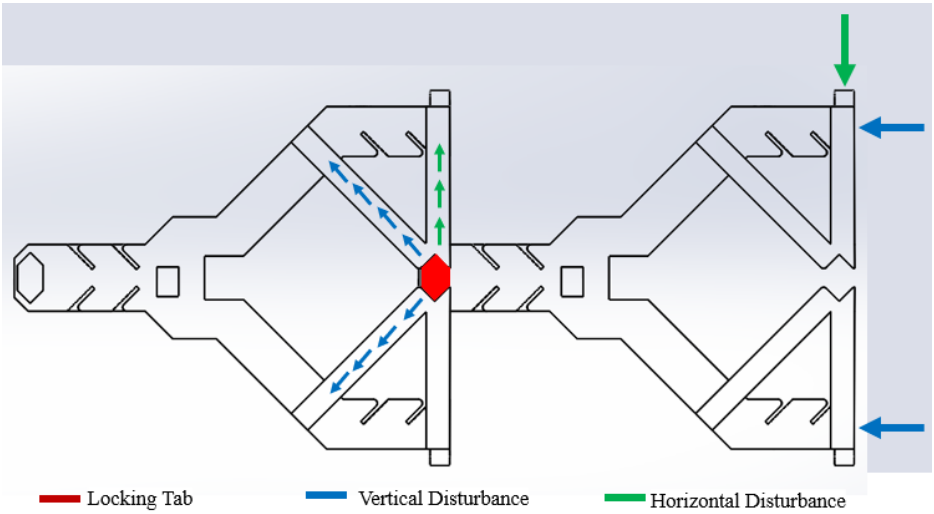

Figure 3.2: Locking arm design and load distribution.

The locking notch has a hexagonal shape. Average unlocking force testing for different locking designs can be found in Appendix C. The angle of the edges where the notch mates with the locking arms is 45 degrees. This decision is twofold. This allows the faces of the notch to transfer forces to the 45-90 degree locking arms better. Also, increasing this angle would create a steeper angle for the locking notch plane to interact with the locking arm plane. A smaller surface area would be created and less friction on the surfaces would decrease the unlocking force. Decreasing the angle would create a flatter angle for the notch plane to interact with the locking arms plane, making it harder for locking notch to slide out of the grips of the locking arms. This would also increase the surface area of the notch and create more frictional force to keep the notch in the

locked position. The notch thickness can change the unlocking force of the mechanism. Decreasing the thickness of the notch in the x direction would bring the critical point of the notch closer the end of the locking arm, allowing less deflection to unlock. Increasing the thickness of the notch would increase the amount of deflection experienced by the locking arms and make it harder to unlock.

Flexural Members

The flexural members serve a critical role in the bistable characteristics of the actuator. The flexural member takes the shape of a slender beams because of its post buckling characteristics. The three dimensions that make up the flexural are the length, width, and thickness. The width of the flexural was kept constant with the 5mm width of the frame. The length dimension drove the testing for the actuator because of its effect on changing the slenderness ratio. To create the assumption of a fixed-fixed configuration of the flexural, the member needed to be press fit into the flexural slots. Each flexural slot is 2.5mm long and add to the supported length of the member. The unsupported length of the member is that part of the beam that is not fit into the slot. The unsupported dimension will be referred to as the length of the flexural member. Thickness is a critical dimension because it significantly changes the area moment of inertia of the member. Thickness considerations are further explained in the material considerations section.

Configurations

The frame and flexural members are designed to serially connect modules of actuators that can create multiple configurations. A bistable mechanism is made when the flexural members are combined with the frame; the mechanism can remain in an extended (1) position or a compressed (0) position without the need an external force. This allows the configurations to be describe as a binary sequence. The extended position takes advantage of the structural rigidity of the straight flexural members and the compressed position takes advantage of the post buckling soft characteristics. The buckled flexural members will take a double curve shape that represents the second mode of buckling. The number of configurations of a robotic arm can be calculated using:

$$N = 2^n \tag{3.3}$$

where N is the number of configurations, n is the number of actuator modules used in the arms, and the 2 represents the bistability of the actuator. Figure 3.3 displays the four configurations of a two-module arm. The four configurations create three unique lengths of the two-module structure. The 11 configuration is not meant to rotate. The 01, 10, and 00 each have a unique reach when a moment is applied to rotate the 0 joint.

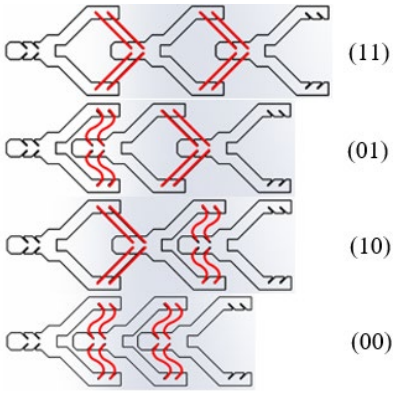

Figure 3.3: Four configuration of a two-module robotic arm

Figure 3.4 displays a two-module arm in an ideal 90-degree configuration. In this design, each 0 module ideally allows a 0-to-45-degree rotational range. The angle of rotation is controlled by a changing tendon length that will be talked about in the robotic arm section. This is due to the changing buckling modes of the flexural members. The members on the inside of the 90-degree rotation remain in the second, double curve buckling mode, while the outer members transition back to the first buckling mode under.

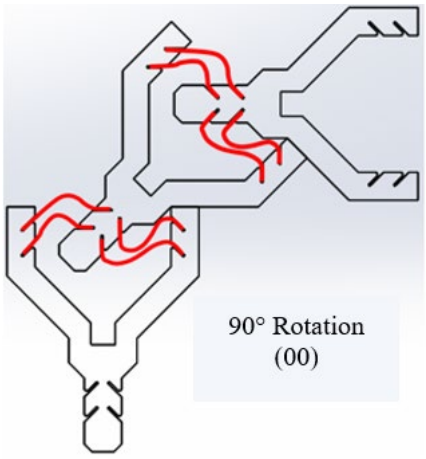

Figure 3.4: Max ideal rotation of a (00) two module actuator.

Fabrication

One compliant unit actuator module consists of two frames, four flexural members, and four pins. Each component is made from a different material using different fabrication processes. Each module is designed to be strong and flexible. Material strength is defined by the yield strength or the ultimate strength. The flexibility is defined by material stiffness or Young's Modulus [31]. In choosing a material for the frame and flexural members, the Strength to Young's ratio was calculated for a variety of materials. A large value for this ratio indicates that a material can be strong compared to the stiffness that material possesses. Various material properties and considerations can be found in Appendix D [32-34].

The frame of the mechanism was made of Clear V4 Resin from Formlabs. This provided a rigid frame that was flexible enough to create the deflections needed to unlock the frame and produce a snap through buckling. This material is also closest to polypropylene, which is the recommended compliant mechanism frame material. The flexural members are made of high-density polyethylene (HDPE). HDPE kept the flexural members sturdy in the 1 position and capable of soft movements in the 0 position. Thickness of the flexural members was a critical dimension that drove material decisions. The thickness of the flexural members is 0.55mm. Increasing the thickness of the flexural caused significant plastic deformation in the first and second buckling modes. Images of the plastic deformation differences in 0.55mm, 0.63mm, and 0.80mm

thicknesses can be seen in Appendix D. The assembly pins were made of thin galvanized steel wire. The pin material needed to be rigid enough to push through the frame pinholes and keep the supported flexural member length mated to the frame.

The frame was fabricated using a Formlabs Form 2 3D printer. Its 14.5cm by 14.5cm printing area was capable of printing multiple unit actuator frames through the stereolithographic (SLA) printing process. The frame was modeled in Solidworks, laid out for printing in Preform. The frame was printed so that the XY plane of the frame was on the surface of the printer. This allowed the layers of the SLA printer to build in the Z direction. This layout was chosen because it prevents the layers from being printed in the same plane that the frame arms were bending [35]. If the printed layers were in the same plane as the arm, bending stresses would be magnified and the actuator frame would approach failure quickly.

When each of the components are fabricated, assembly can take place. First, slide one side of flexural members into the slots located on the frame base. Once the flexural members are inserted all the way in, slide the pin into the pinhole on the frame and through each of the slotted flexural members. Repeat this step for the other side of the base. Next, slide the other end of the flexural members in the slots on the frame arm. Once the flexural members are fully inserted, slide the pin into the pinhole on the frame arm and through the two flexural members. Repeat this step for the other side. While sliding the flexural members into the frame arm, align the locking tab into the locking

notch for easier precise assembly. Figure 3.5 displays an exploded view of the assembly components and a fully constructed two module assembly. With the actuators fabricated and assembled, testing and validation procedures could occur.

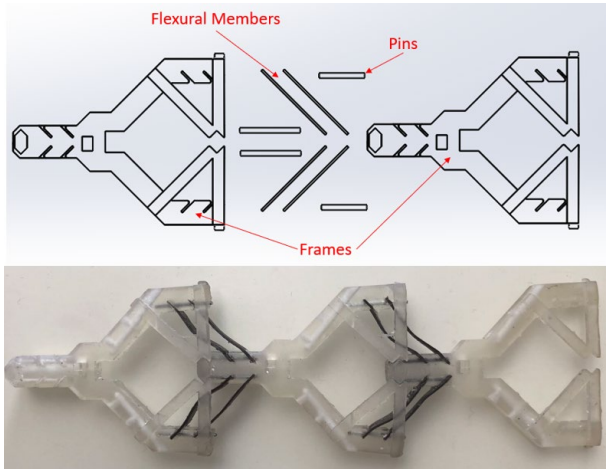

Figure 3.5: Assembly components a) Exploded and labeled view of single unit actuator and b) Two module actuator assembly.

CHAPTER FOUR

ACTUATOR EXPERIMENTAL TESTING AND RESULTS

Three main tests were used to analyze and validate the compliant unit actuator: the cycle test, the unlocking test, and the bending test. Each of these tests were used to measure stroke, unlocking force, variable bending stiffness, and other design characteristics used in the robotic arm.

Cycle Test

The cycle test was used to prove the bistability of the actuator, measure the stroke, and determine critical values along the hysteresis loop. It was used to analyze the flexural length as a critical dimension. A hysteresis loop is fundamental in describing the loading and unloading conditions of an actuator. The cycle test is a displacement control test. The actuator experiences a compressive load along the y axis that displaces the actuator until the loading is reversed to a tensile loading that brings the actuator back to its original position. This process represents one cycle. The compressive and tensile loads are recorded and used for analysis.

Setup

The equipment used in the displacement-controlled testing was an Admet Material Test machine, an Admet 25lb load cell, a cycle test fixture, a unit actuator, and a base fixture. The experimental setup is displayed in figure 4.1.

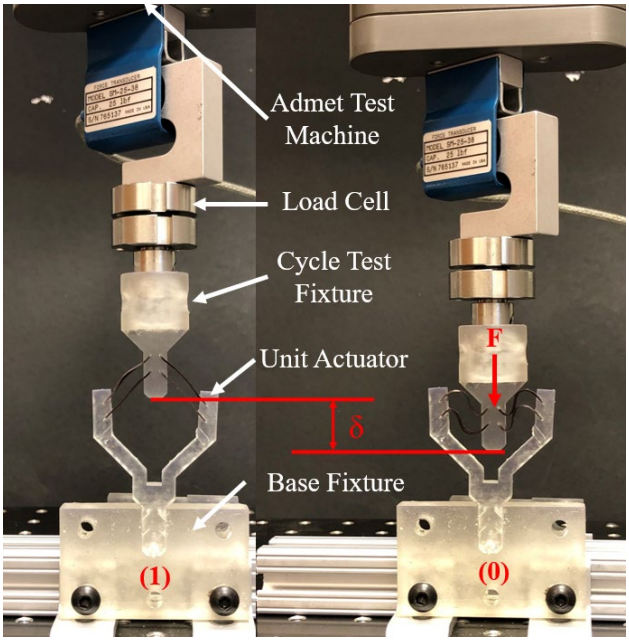

Figure 4.1: Testing setup for the actuator cycle test. The actuator was attached to a load cell with a cycle fixture to measure the compression and extension load conditions.

Three actuator configurations were tested: an actuator with a 15mm flexural length, a 18mm flexural length, and an 21mm flexural length. The thickness of the flexural members was 0.55mm for each configuration. The only change in the frame for each actuator was an increased base width to accommodate the shorter flexural lengths. The length and thickness of the frame arms remained constant. A custom cycle test fixture was developed for each configuration. This fixture mimicked the base of a unit actuator and connected the actuator to the load cell. A base fixture was designed for each configuration. This case feature kept the unit actuator specimen in a fixed position. It was designed in a way such that the frame arm deflection was not affected by fixing the base to the ground.

Method

The unit actuator undergoing testing was assembled to the test fixture as described in the assembly process. The cycle test fixture was then slid onto the loadcell and secured with a pin and fixture nut. Once the actuator and fixture were secured, the testing machined was zeroed to provide accurate load measurements. The actuator was then lowered and pressed into the base fixture. At this point the load readout expressed a non-zero reading because of the downward displacement of the actuator. The position of the actuator was adjusted until the load readout was zero. The machine was zeroed again, now with the correct origin position and zero load. With the actuator secured and the machine zeroed, the cycle test could be initiated.

The test consisted of 10 continuous cycles. Each test displaced the actuators at a rate of 25.4mm/min. The 15mm configuration was displaced 20.5mm, the 18mm configuration was displaced 22mm, and the 21mm configuration was displaced 24mm. The lengths were changed because of the unique stroke value for each configuration. Making the cycle too short could reduce the measured stroke and influence the bistability and making the cycle too long could induce unwanted stress by pushing the actuator past its stable position and creating an increasing stress on the flexural members and induce failure. Critical positions along the hysteresis cycle that were calculated were locations of maximum force, minimum force, and zero force.

With the critical values, data was calculated to find the stroke length and the total cycle energy. The stroke was calculate using equation 4.1. The stroke length was compared to an ideal stroke. The ideal stroke is calculated with based on the assumption that the flexural lengths remain straight in the extended and compressed position. The ideal stroke equation is:

$$\Delta x_i = 2L \sin\theta \tag{4.1}$$

where Δx_i is the ideal stroke and θ is the 45° flexural angle. The ideal ratio equation is:

$$S_i = \frac{\Delta x}{\Delta x_i} \tag{4.2}$$

where S_i is the unitless comparison between calculated stroke and the ideal stroke. The length ration equation is:

$$S_l = \frac{\Delta x}{l_t} \tag{4.3}$$

where S_l is the unitless comparison between stroke and l_t is the total length of the unit actuator module, 103.7mm.

The total cycle energy was calculated by taking the integral of the curve with the trapezoid method to find the total area under the cycle curve:

$$E = \int_{x_{s1}}^{x_{s2}} f(x)dx \approx \sum_{x_{s1}}^{x_{s2}} \frac{x_n - x_{n-1}}{2}[f(x_{n-1}) + f(x_n)] \tag{4.4}$$

where E is the total energy of the cycle and $f(x)$ is the force displacement curve.

Results

A hysteresis loop was developed to show the loading and unloading conditions of each unit actuator. The force versus displacement curves for each flexural length is displays in figure 5.2. The green line represents the first cycle initial loading. The blue line represents the average loading for following nine cycles. The red line represents the average unloading for the following nine cycles. The critical points for each of the ten cycles were not significantly affected by the standard deviation, so the average value plot is an accurate representation. The four critical points measured were the local maximum loading, the local minimum unloading, the first zero of the loading line, and the third zero of the unloading line.

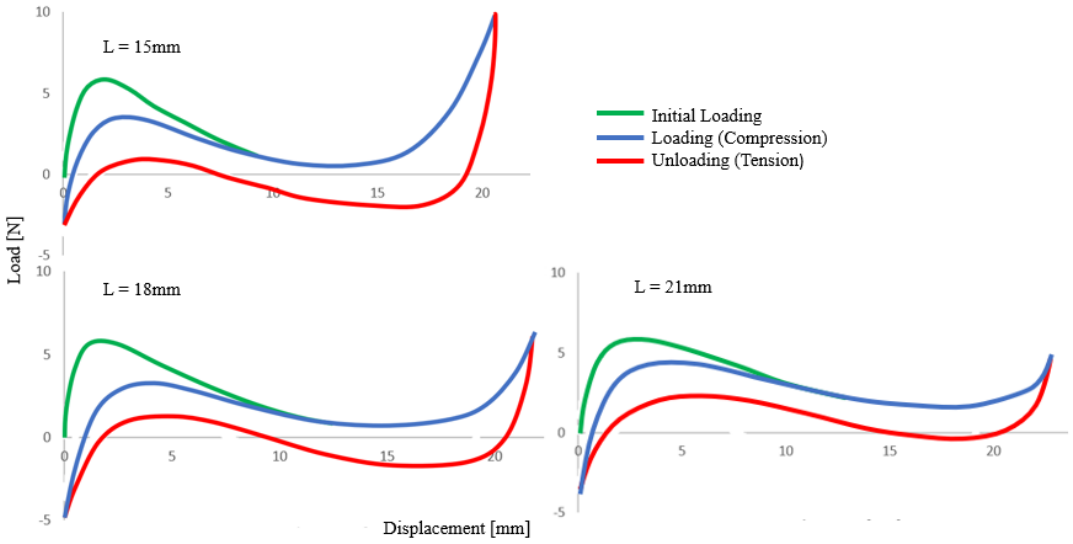

Figure 4.2: Loading and unloading cycle values for the 15mm, 18mm, and 21mm actuators.

The maximum loading and minimum unloading measurements are displayed in Table 4.1 The 15mm actuator experienced the greatest compressive load at 3.925N at the shortest loading displacement of 2.911. The 15mm actuator also experienced the greatest tensile load at 1.99N at the shortest unloading displacement. The 21mm actuator experienced the smallest tensile load of 1.46N at the longest displacement of 17.99mm. Between the 15mm and 18mm actuators, there is a 0.52N difference in compressive load, while there is only a 0.22N difference between the 18mm and the 21mm actuators. Both the 18mm and 21mm actuator have slenderness ratios over 100 and the 15mm actuator does not. There is a 0.065N difference between the compressive loads of the 15mm and 18mm actuator, while there is a 0.471N difference in compressive loading between the 18mm and 21mm actuator. The maximum compressive load, F_{max}, is greater than the maximum tensile load, F_{min}, for each actuator. This shows that the actuator is more stable in the extended position than it is in the compressed position.

Table 4.1 Critical loading and unloading results from the actuator 10 cycle test.

L [mm]	λ	F_{max} [N]	x_{max} [mm]	F_{min} [N]	x_{min} [mm]
15	94.48	3.92	2.91	-1.99	16.76
18	113.37	3.20	3.60	-1.93	16.99
21	132.27	3.42	3.97	-1.46	17.99

The critical calculations for the zeros are displayed in Table 4.2. The 15mm actuator had the shortest stroke length at 18.62mm and the 21mm actuator had the longest stroke length at 20.51mm. The 15mm actuator required the most energy, 0.057 J, to

complete a compression and extension cycle and the 21mm actuator required the least amount of cycle energy, 0.041J. When comparing the differing stroke to the total length of the unit actuator, each configuration had a stroke around 18% of the total length. The ideal stroke ratio shows how much of the stroke measurement is coming from the length of the flexural member. The 15mm actuator has the greatest ideal stroke ratio meaning the buckled flexural members give a stroke that is 88% of a traditional link that does not buckle and does not produce a curvature. As the slenderness ratio increases, this ratio decreases, about 10% for every 3mm. Although the 21mm actuator has the longest stroke, it is not fully utilizing the entire length of the flexural member.

Table 4.2 Critical stroke results from the actuator 10 cycle test

L [mm]	λ	E [J]	Δx [mm]	Δx_i [mm]	S_i	S_l
15	94.48	0.057	18.62± 0.06	21.21	0.88	0.18
18	113.37	0.042	19.30 ± 0.23	25.46	0.76	0.19
21	132.27	0.041	20.51 ± 0.12	29.70	0.64	0.18

Discussion

A slenderness ratio over 100 can create predicted buckling failure. The three actuator lengths were picked to show a slenderness ratio just under 100 and two ratios that exceed 100. The values with the larger slenderness ratio will buckle and create a larger curved shape than those of smaller slenderness ratios. When the S_i is decreasing, this shows that the actuator is pushing the flexural members deeper into the second buckling mode. Figure 5.3 displays samples in the compressed stable position and the varying flexural curvature.

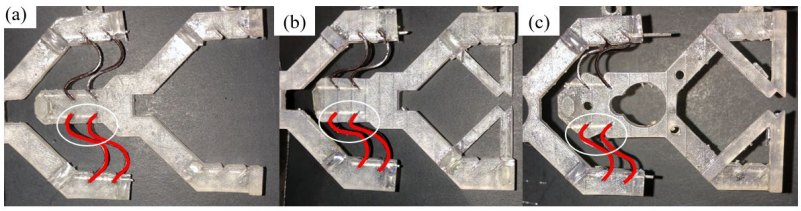

Figure 4.3 Unit actuators in the compressed stable position. The buckled flexural members highlighted for the a) 15mm actuator, b) 18mm actuator, and c) 21mm actuator.

One of the main weaknesses in compliant mechanism is failure due to fatigue. The more a flexible piece of plastic bends, the greater amount of fatigue and plastic deformation it will experience. This experiment showed that a critical failure position on the unit actuator is where the flexural members attach to the base of the frame. The flexural members experience the greatest deformation at this area. In figure 5.3, the highlighted flexural members show that the 18mm and 21mm actuators have a greater curvature around the base frame slots than the 21mm actuator. During experimental trials for the cycle test, the actuators failed mostly in this location. More of the failures occurred with the shorter flexural lengths. Not all the flexural members would fail at once, typically just one per testing cycle. Even though a flexural member may break during a cycle test, it was discovered that the remaining functional components of the actuator would exhibit bistability.

To reduce the fatigue on the flexural members and increase the expected cycle life, a radius was designed into each of the flexural slots. Figure 4.4 displays the difference between an edged flexural slot and a radius flexural slot. The radius was meant

to decrease the curvature of the flexural member at the frame base location by increasing the radius of the first curve in the flexural member. The radius on the frame increased the contact surface area between the flexural member and the frame. This helped decrease the curvature and reduce the stress at that location. An edged corner created too much of a concentrated force that increased the flexural stress at base location of the frame, especially during the loading and unloading cycle of the 15mm and 21mm actuators. After this feature was added into the design of the frame before the final cycle test was executed.

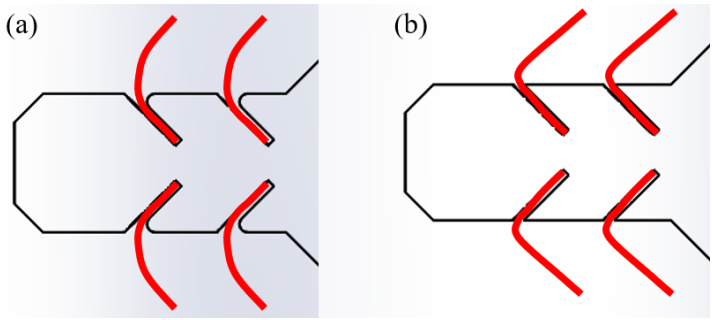

Figure 4.4 Curvature reduction in the base of the frame design, a) the radius design decreases curvature by increasing the flexural bend radius and b) the edge design increases curvature by decreasing the flexural bend radius.

The cycle test also showed that a shorter flexural length will give the actuator greater load performance. The maximum force of the 15mm actuator made it the most resistance to compressive loads in the extended position. The minimum force of the 15mm actuator made it the most resistant to tensile loads in the compressed position. These two features caused the 15mm actuator to consume the most energy to while

transitioning from the stable extended equilibrium and snapping through to the stable compressed equilibrium. Although the 15mm actuator had slightly better load performances than the others, the 21mm actuator exceeded each of the other two in stroke and showed that an increased flexural length may reduce the fatigue in the flexural members because of the decreased curvature at the base of the frame.

Bending Test

The bending test was used to prove the variable stiffness tuning of the actuator by measuring the force and displacement through a cantilever beam setup. This test was also used to determine the most effective extended stiffness to compressed stiffness ratio. It was used to analyze the flexural length as a critical dimension. A bending moment curve is fundamental in describing the bending stiffness of a robotic arm module. The bending test is a displacement control test. The actuator experiences a compressive load along the x axis that displaces the actuator to create a displacement angle of rotation. The compressive load and displacement measurement were measured and used for analysis.

Setup

The equipment used in the displacement-controlled testing was an Admet Material Test machine, an Admet 25lb load cell, a cycle test fixture, a unit actuator module, and a base fixture. The experimental setup is displayed in figure 4.5.

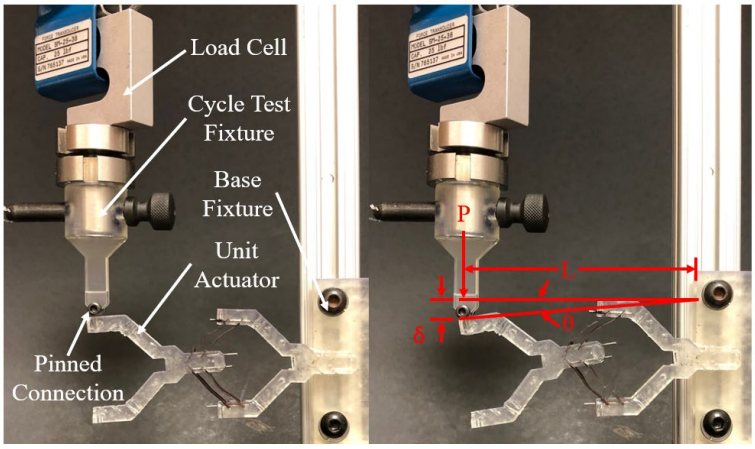

Figure 4.5: Testing setup for the actuator bending test. The actuator was pinned to a load cell with a fixture to accurately measure the force acting on a constant point of the actuator.

Three actuator configurations were tested: an actuator with a 15mm, 18mm, and 21mm flexural length. The thickness of the flexural members was 0.55mm for each configuration. The only change in the frame for each actuator was an increased base width to accommodate the shorter flexural lengths. The length and thickness of the frame arms remained constant. A custom cycle test fixture was developed for each configuration. One end of the fixture attached to the load cell and another end attached to the side of unit actuator frame arm. The fixture attached to actuator arm with a pinned connection to precisely load the actuator module without the test fixture slipping along the side of the frame. A base fixture was designed for each configuration. This case feature kept the unit actuator specimen in a fixed position. It was designed in a way such that the frame arm deflection was not affected by fixing the base to the ground.

The unit actuator module was assembled according to the process in the assembly section. The test fixture was then pinned and secured with the fixture nut to the load cell. A pin was used to attach the fixture to an extruded loop on the side of the end frame arm. The test machine was then zeroed to accurately record load values. The base fixture was bolted to the test machine a specific length away from the load cell to ensure the actuator module was in the exact stable position. This length varied with each actuator module because of its overall length. The position of the base aligned the actuator module directly under the load cell, ensuring a central load. After this, the actuator module was secured into the base fixture. The position of the load cell was adjusted until the unit actuator was perpendicular to the test load fixture and the load reading was zero. With the actuator secured and the machine zeroed, the cycle test could be initiated.

Method

Six configurations were used in the bending test. The 14mm flexural actuator, the 16mm actuator, and the 18mm actuator were all tested in the 1 and 0 position. A 5mm downward displacement was applied to the unit actuator at a rate of 25.4mm/min. This process was repeated five times per configuration. Once the force and displacement values were recorded, the effective bending stiffness was calculated by:

$$K_B = \frac{M}{\emptyset} = \frac{FL}{\tan^{-1}(y/L_B)} \tag{4.5}$$

where K_B is the effective bending stiffness, M is the applied moment, $\emptyset$ is the rotation angle, F is the reaction force, y is the downward displacement, and L_B is the lateral distance between the applied force and the axis of rotation. To analyze the performance of each unit actuator module, the bending stiffness ratio was calculated using:

$$K = \frac{K_1}{K_0} \tag{4.6}$$

where K is the bending stiffness ratio, K_1 is the bending stiffness in the extended stable state, and K_0 is the bending stiffness at the compressed stable state.

Results

The applied moment versus bending angle was plotted for the compressed and extended position for the 15mm, 18mm, and 21mm actuators. Figure 4.6 displays the results for each of the bending test. The green data lines show the bending tests in the extended position and the yellow lines show the bending tests in the compressed position.

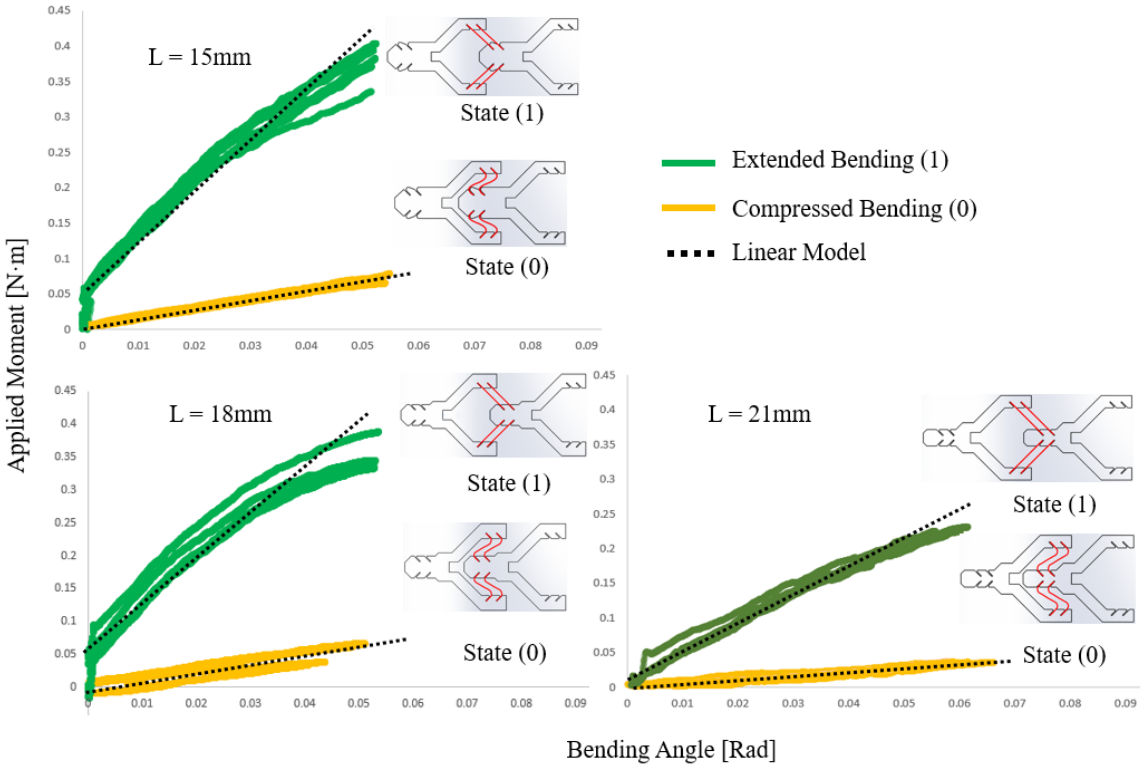

Figure 4.6: Applied Moment [N-m] vs Bending Angle plot for the 15mm, 18mm, and 21mm actuator. Each actuator length was tested in the extended position (1) and the compressed position (0)

The largest extended bending stiffness ratio was the 15mm actuator, 6.494 N·m/rad and the smallest compressed bending stiffness ratio was the 21mm actuator at 0.593 N·m/rad. The stiffness trends stay consistent with the slenderness ratio: as the slenderness ratio increases, the K_{B1} stiffness will increase and the K_{B0} stiffness will decrease. Although the 21mm actuator had the smallest K_{B1} value, its bending stiffness ratio was the largest. Figure 4.4 shows that the bending results for the 21mm actuator with the most linear trend. Since the bending stiffness calculation, the slope of each line,

the bending stiffness with the smallest variance will be the most repeated linear line. The extended position bending results show a stronger nonlinear response compared to compressed position.

Each of the extended positions show a larger resistance to small end moment loads. The moment to bending angle relationship becomes less linear as the end load increases and the actuator deflection surpasses 0.04 Rad. The resistance to rotation decreases causing the bending stiffness to decrease. This proves another advantage to adding the locking mechanism to the actuator frame, which is discussed in the next subsection. One motivation is adding the locking mechanism was to add extra resistance to an increasing end moment load. When the stiffness of the actuator begins to decrease, like in figure 4.4, the locking tab will transfer part of that end lock through the locking arms and into the more structurally supported sections of the frame. This will take away stress from the flexural members and further increase the rigidity of the extended position.

Table 4.3: Critical bending stiffness results for the extended and compressed positions of the actuator bending test.

L [mm]	λ	K_1 [N·m/rad]	K_0 [N·m/rad]	K_{10}
15	94.475	6.494 ± 0.054	1.232 ± 0.214	5.284
18	113.371	5.173 ± 0.380	1.052 ± 0.455	4.916
21	132.266	3.799 ± 0.288	0.593 ± 0.070	6.403

Discussion

The advantage to having an actuator that transitions to a low bending stiffness is to mimic the features of a soft robot. The smaller bending stiffnesses allow the arm to be safer to use and easier to rotate. In the compressed state, the 21mm actuator will exhibit the best soft robotic features. Also, it was discovered during the experiment that the 21mm actuator frame allows for more rotational movement than the 15mm and 18mm actuator. Figure 4.7 displays the rotational space difference during the experiment. The top row shows the actuators in the nonrotated position, and the bottom row shows the actuators rotated five degrees. As the actuator rotates downward, the flexural members on the bottom will experience tension and flexural members on the top will experience compression. As the actuator rotates past 5 degrees, the base frame and the frame arm will start to interfere with the flexural members for the 18mm actuator in figure 4.7b, and the 15m actuator in figure 4.7c. The 21mm actuator in figure 4.7a gives the module more space to rotate, which will prevent the frame from contacting the flexural members. When the frame contacts the flexural members, like the yellow circled area in figure 4.7b, this increases the force needed to rotate the module and will increase the bending stiffness in this configuration. The larger area in the 21mm actuator prevents the two connected frames from making contact during rotation. The wider base frames in figure 4.7b and 4.7c will limit rotation because they will make contact with the connected frame arms, creating more friction and increasing the bending stiffness in the compressed (0) position.

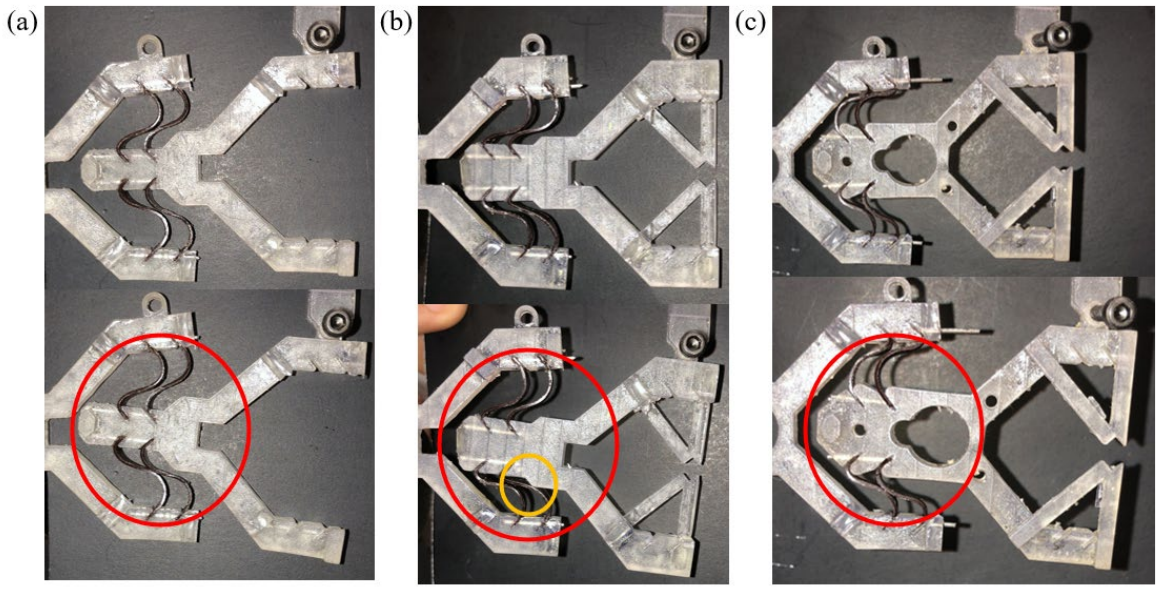

Figure 4.7: Rotational space differences between the a) 21mm actuator, b) 18mm actuator, and c) 15mm actuator.

Going forward with the testing, the 21mm actuator will be used because of the large bending stiffness ratio and the large stroke values. Even though the 21mm actuator does not handle the largest loads and can be pulled out of the compressed stable position with less force, the stroke and bending performance outweigh these short comings. The locking arm layer was used to reinforce the 21mm actuator. These locking arms increased the maximum compressive force the module could withstand and increased the bending resistance under large rotations. The 21mm actuator can be held in the compressed position by the tendons used in the robotic arm construction. The future sections will discuss how some of these shortcomings were addressed and how the robotic arm was designed using the 21mm actuator.

Unlocking Test

The unlocking test was used to measure the unlocking force and the unlocking position of the unit actuator locking mechanism. The unlocking force should be located near the same displacement position as the local maximum of the cycle test. With the layered approach for the mechanism design, the actuator works with and without a locking layer. The locking test shows that the unlocking force will only change the maximum compressive force of the hysteresis loop. The unlocking test was a displacement-controlled test. A compressive load is exerted along the y axis on the unit actuator until the locking arms release the locking notch. The load and displacement were recorded.

Setup

The equipment used in the displacement-controlled testing was an Admet Material Test machine, an Admet 25lb load cell, a load plate, a unit actuator module, and a base fixture. The experimental setup is displayed in figure 4.8.

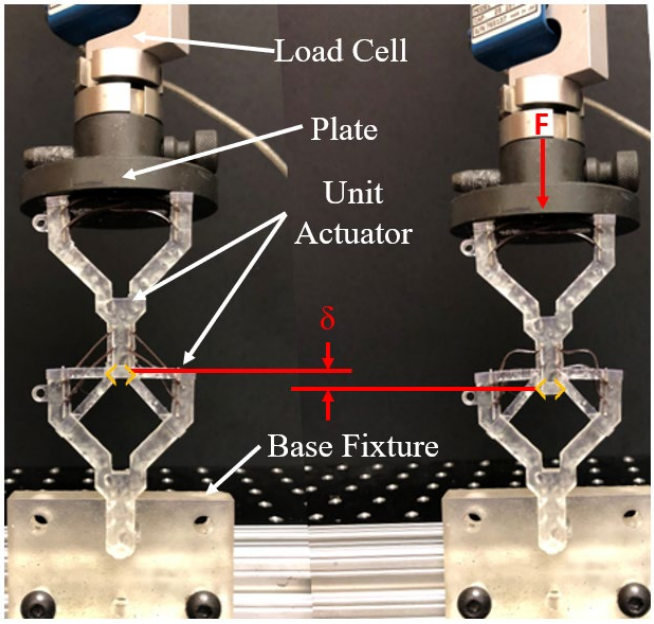

Figure 4.8: Testing setup for the actuator unlocking test. The actuator experienced a compressive force until the locking tab was released from the locking arms on the 21mm unit actuator.

One configuration was tested for the unlocking test. Throughout the cycle testing, the frame arms were not modified in the testing. Since the unlocking force is predicted to be larger than the max compressive force of any of the flexural member configurations, one 18mm actuator configuration was tested. The load plate attached to the load cell with a pin and a fixture nut. The load plate evenly distributed a symmetric compressive load onto the locked actuator. The same base fixture from the cycle test was used to fix the unit actuator to the ground. The fixture did not hinder the deflection of the frame arms.

The unit actuator module was assembled according to the methods described in the assembly section. The load plate was slide onto the load cell and secured with a pin

and fixture nut. The test machine was then zeroed to ensure accurate load measurements. The actuator module was set into the base fixture and positioned directly underneath the load plate. The load plate was then lowered down as close to the frame arms while keeping a zero-load reading. Once the start position was reached, the test machine was zeroed again, now with the correct load and position origin. With the actuator secured and the machine zeroed, the cycle test could be initiated.

Method

Five test cycles were collected for the individual actuator module. Figure 5.6 displays the unlocking process of the test. As the compressive force increases, the locking arms will deflect outward and cause the locking notch to be released by the locking arms. From left to right, figure 5.6 displays the locking tab aligned with the locking notch. Next, a downward force is applied to the actuator module and the locking arms begin to deflect, breaking contact with the locking tab. As the downward force increases, the locking arms deflect outward, and the locking tab will slide down the incline of the locking notch. The combination of the locking arm deflection and the locking tab sliding down the incline will exceed the limits of the locking notch and release the locking tab to a position below the locking arms. The actuator is now able to transition into the compressed position. The force measurements of the test will reveal the maximum force the actuator experiences, the unlocking force. The displacement measurements will reveal the exact unstable location that the actuator snaps from an extended position to a

compressed position. The ratio of the unlocking force and the local maximum cycle force was calculated using the equation:

$$S_L = \frac{F_{Max}}{F_{Unlock}} \tag{4.7}$$

where S_L is the ratio of the unlocking force to the maximum cycle force, F_{Max} is the local maximum cycle force, and F_{Unlock} is the unlocking force. The ratio of the unlocking force to the module weight was calculated using the equation:

$$S_W = \frac{F_{Max}}{W_{Module}} \tag{4.8}$$

where S_W is the unlocking force to the weight ratio and W_{Module} is the weight of an actuator module, 0.187N.

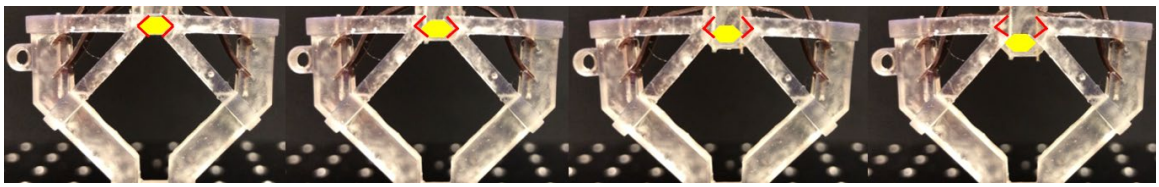

Figure 4.9: The four-step unlocking process. First, the locking notch rests in the locking arm cutout. Second, a compressive downward force pushes the locking arms away from the locking notch. Third, the compressive force reaches a maximum where the locking notch is at the edge of the locking arm cutout. Lastly, the locking notch is completely displaced from the locking arm cutout.

Results

The results of the unlocking test are shown in table 4.4. The 21mm actuator will unlock after an 18.434N compressive load. The unstable unlocking position occurred at a

displacement of 3.266mm. The locking mechanism allowed the actuator module to carry over five times the compressive loading at a frame without the locking mechanism, tested in the cycle test. The locking mechanism also allows the actuator module to withstand a compressive load almost 100 times its own weight.

Table 4.4 Critical force results for the 21mm actuator unlocking test.

L [mm]	F_{Unlock} [N]	x_{Unlock} [mm]	W_{Module} [N]	S_L	S_W
21	18.434 ± 1.854	3.266	0.187	5.384	98.676

Discussion

The cycle maximum force was 3.424N and located at a displacement of 3.971mm. With this design, the actuator unlocks at a position close to the local maximum force which proves two critical approaches to the actuator design. During the unlocking process, the actuator is utilizing the dynamics of its own frame to unlocking, not just surface friction. If the unlocking position were at a shorter displacement, like 1.5mm, the unlocking transition would not be efficiently utilizing the deflection of the frame and transferable force of the flexural members. The locking tab would be pressed downward on the locking notch until the pressure increased too much or until the locking arms failed. The local maximum force location from the cycle test provides an ideal deflection location for the locking arms to release the locking tab from the locking notch. If the unlocking were at a larger displacement position like 5.5mm, the same failure could happen. The locking arms would not experience the adequate displacement and the

friction created between locking tab and the locking from the downward force would induce a frame failure.

The locking ratios show the advantages of using actuator modules for a robotic arm. A single actuator module can support almost 100 times its own weight. This allows an end user to have flexibility when choosing an end effector to put on the robotic arm. An end effector made of similar material to the actuator module may not weight 100 times more than the actual arm module, but this also increases the load capacity of the arm module.

CHAPTER FIVE

ROBOTIC ARM DESIGN

Construction

The robotic arm fabricated in this study was comprised of three compliant mechanism unit modules. The modules utilized the 21mm actuator frames. This frame size was chosen because of the large stroke length and the high bending stiffness ratio. This ratio is critical for a robotic arm that functions like a soft robot. Figure 5.1 displays the proof-of-concept robotic arm. The arm was mounted to a quarter inch thick plexiglass plate, where a frame actuator fixture provided a base that bolted the robotic arm to the plexiglass plate. On top of the plexiglass plate, two 12-volt Tsiny gearbox motors were powered by a power supply set to 12V and 0.1A. Braided thread was woven through the frames of each actuator module, this type of thread was assumed to be inextensible so that the tendon control would be precise. There are two sets of tendons, one on the left side of the robot and one on the right side of the robot. A spine is used to manipulate the three modules. The spine can be pushed through each of the spine guides, where the tab of the spine can rotate into the notch of the frame.

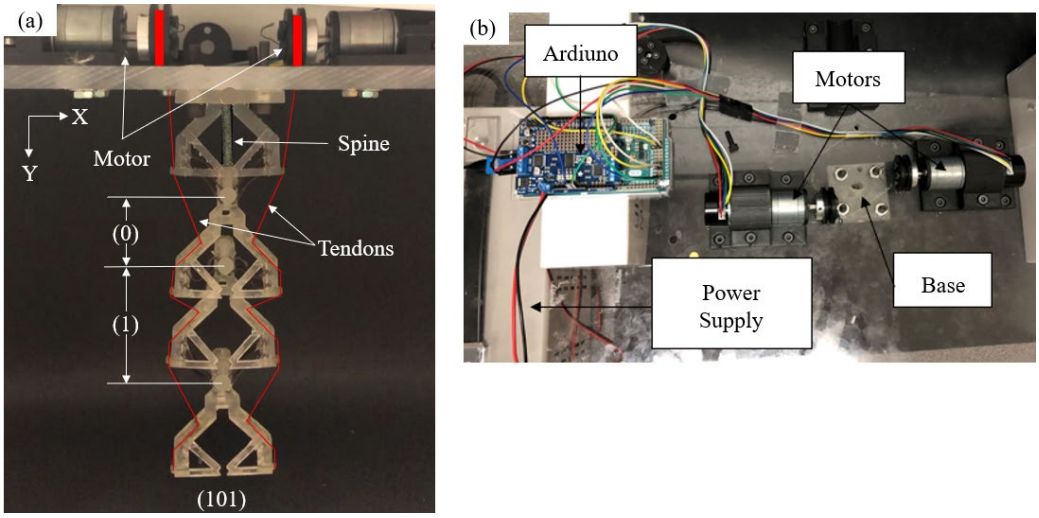

Figure 5.1: Robotic arm construction: a) Front view of the three-module arm in the 101 configuration. b) Top view of the experimental setup plexiglass top mount

Configurations

The robotic arm is set in the designated configuration by a user who manipulates the spine. The arm is constructed in the 111 configuration and all other configurations must originate from this initial configuration. Table 5.1 displays the transformation map. A module going from 0 to 1 is an extension and a module going from 1 to 0 is a compression. The first digit is the module at the base of the arm and the last digit is the module at the end of the arm.

Table 5.1 Configuration transformation map for a three-module robotic arm

Configuration	Sequence
111	Initial Configuration
100	111→011→001→000→100
110	111→011→001→000→100→110
101	111→011→001→101
000	111→011→001→000
001	111→011→001
011	111→011
010	111→011→001→000→100→110→010

The act of compressing a module is easier done when there is a compressed module in front of it. For example, 011 to 001 shows that the second module is compressed, while the first module stays compressed. Trying to compress a module with an extended module before it may cause both the modules to compress. For example, 110 to 100 may introduce error because of the possibility of the increased compressive force compressing the first two modules, 110 to 000. Likewise, the act of extending a module is easier done when there is an extended module in front of it. For example, 100 to 110 shows that the second module is extended, while the first module stays extended. Trying to extend a module with a compressed module before it may cause both the modules to extend. For example, 001 to 011 may introduce error because of the possibility of the increased tensile force to extending the first two modules, 001 to 111. These two factors make the transformation of the first module important in each of the transformations. Once the robotic arm is set in the desired configuration, the tendons can be manipulated to rotate the arm. Figure 5.2 displays the transformation and rotation of the 101 configuration.

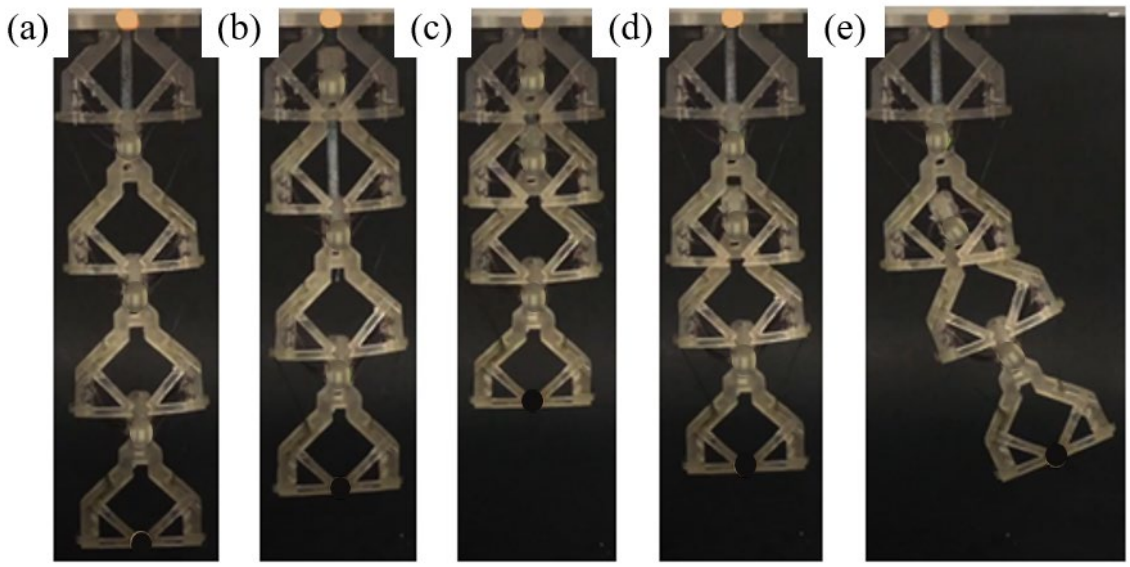

Figure 5.2 Transformation and rotation of the 101-configuration: a) The robotic arm starts in the initial 111 configurations. b) The spine compresses the first module into the 011 configuration. c) The spine compresses the second module into the 001 configuration. d) The spine extends the first module into the 101 configuration. e) The left tendon becomes longer, and the right tendon is pulled shorter as the arm rotates to the right.

The robotic arm begins in the 111 configurations. The user then manipulates the spine by hand through the first frame. A detailed figure of the spines notch and frames can be found in Appendix A. Once the notch of the spine is level with the notch cut out in the frame, the user rotates the spine 90 degrees counterclockwise to lock the spine notch into the frame. The user then pulls the spine up, compressing the module that the notched frame is attached to. After the desired module is compressed, the user rotates the spine 90 degrees clockwise to release the spine notch from the frame's notch cut out. This process is repeated for the second compressed module. For the extension of the first module, the

user manipulates the spine the same way as before. Instead of pulling to compress the module, the user will push down on the spine to extend the notched module. Once the module is extended the user rotates the spine clockwise 90 degrees to unnotched the frame. Now the spine can be retracted to the first extended module to increase the rigidity of the arm base. Once the arm is in the 101 configurations, the tendon lengths are changed to rotate the arm.

CHAPTER SIX

ROBOTIC ARM EXPERIMENTAL TESTING AND RESULTS

Configurations Test

Eight configurations were tested in the configurations test. The robotic arm had three-unit actuator modules. Throughout the test, five significant locations were measured by putting high visibility markers on the arm and taking photos at each configuration. The changes in configuration were controlled manipulating the spine by hand. Once the arm was in the desired configuration, rotation was controlled by changing the length of the two tendons. When both tendons change at the same distance, the tendons lengths remain in sync with the spine configuration change. When one tendon changes to become longer and the other changes to become shorter, this controls the rotation of the robotic arm. The tendon that becomes shorter will define the direction the arm will rotate.

Setup

Figure 6.1 displays the robotic arm configuration test setup. A unit actuator base was used to mount the robotic arm to the testing surface. Three more frame elements were connected in series to create three-unit actuator modules. Marker A is the origin and was placed at the base of the robotic arm. Markers B, C, and D were placed on the frame at the center of the locking notch. This location is closest to the geometric axis of rotation for each of the individual frame. Marker E was placed at the end of the robotic arm. This position represents the mounting position of an end effector. The robotic arm started in

the 111 position. A user needs to manipulate the spine into the desired location before the rotational transformation can occur.

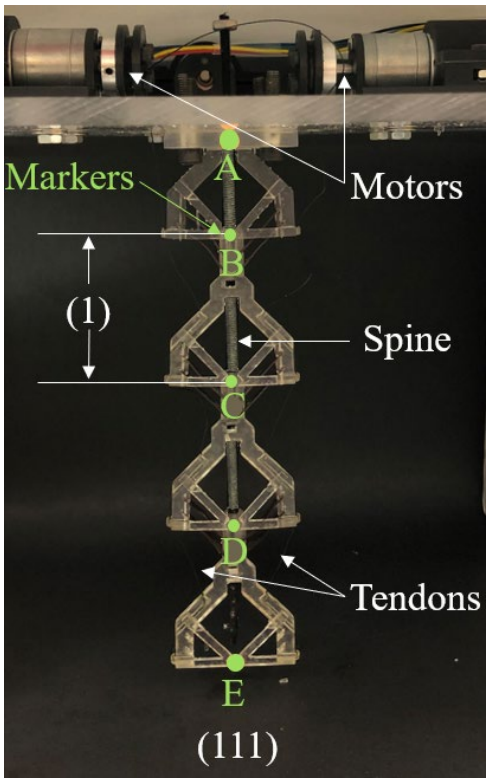

Figure 6.1: The starting 111 position of each actuator configuration. Each critical position was marker with a bright green marker.

Methods

The main control input for the configuration tests was the change in tendon length. The tendons will change according to the function:

$$\Delta l_t = n_0 \Delta l \tag{6.1}$$

where Δl_t is the total change in tendon length, n_0 is the number of compressed modules, and Δl is the change in tendon length to rotate one compressed module. The right tendon will shorten, and left tendon will lengthen by the same length; this will cause the compressed modules of the arm to rotate to the right. The change in tendon length for a single compressed module was calculated using the geometry of the frame. A main line of the tendon is threaded through the frame arm. Pulling the tendon through the frame arm generated the required moment to rotate a compressed module. Figure 6.2 displays the rotation progression according to the changing tendon lengths.

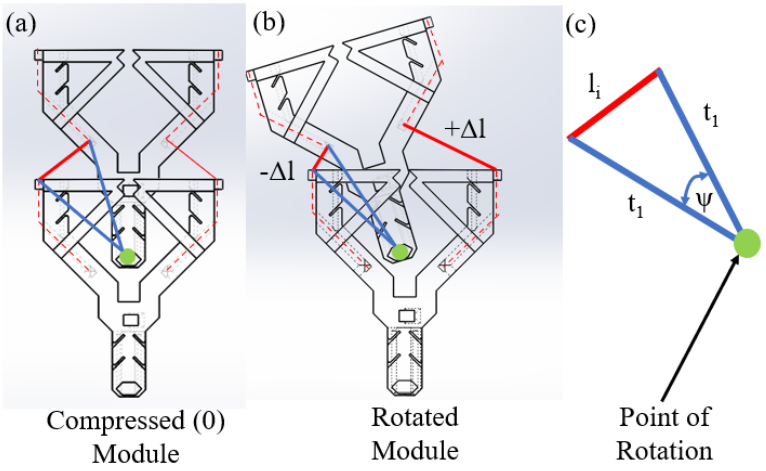

Figure 6.2: Rotation progression of a (0) module, red lines show the tendons and blue lines show critical frame dimensions. a) A compressed module with no change in tendon length. b) A rotated module where the left red tendon is shortened, and the right red tendon is lengthened. c) The triangle and rotation angle create by the tendon actuation

The critical dimensions of the frame, blue lines in figure 6.2, and the tendon length connecting the two frames, red line in figure 6.2, create a triangle that can be used to predict the angle of rotation. The law of cosine was used to solve for the angle of

rotation. It was assumed that the blue line dimensions remained constant during rotation, this allowed the calculation to be controlled by a single input, change in tendon length.

The angle of rotation was calculated using the equation:

$$\psi = \cos^{-1}\left(-\frac{{l_i}^2 - {t_1}^2 - {t_1}^2}{2{t_1}^2}\right) \tag{6.2}$$

where ψ is the angle of rotation, l_1 is the non-rotated length of the tendon, 11.18mm, t_1 is distance between the point of rotation and the tendon hole in the side of the frame arm, 31.39mm. This length acts as a radius because it is assumed that the (0) module will rotate with a constant curvature. To allow for clearance between the two frames as the module rotates, the tendon length was set to change by 10mm. This change predicted that the actuator module will rotate 20.5 degrees. The change in tendon length, Δl, controls the angle of rotation. To rotate an actuator module by a smaller angle, input a smaller change in tendon length. To rotate an actuator module by a larger angle, input a larger change in tendon length. The actuator module does have a rotation limit of 25 degrees. When the limit is reached, the flexural members will experience increasing tension instead of compression, which will force the actuator out of the compressed, buckled stable state. To remain in a stable position, rotation must not exceed 25 degrees per module.

The transformation and rotation process were tested for all 7 rotational configurations. The position of each colored markers was accurately measured using a image processing software. These positions were compared to the kinematic model of the robotic arm. The kinematic model in this experiment utilizes the Denavit-Hartenberg (DH) convention, which represents the transformation of coordinates from the reference frame attached from one unit actuator module to another [36]. The transformation of reference frame A to frame B is calculated with the matrix:

$$H_B^A = \begin{bmatrix} R_B^A & o_B^A \\ 0 & 1 \end{bmatrix} \tag{6.2}$$

where H_B^A is the transformation matrix from A to B, R_B^A is the 3 x 3 representing the rotational transformation from A to B, and o_B^A is the 3 x 1 column vector representing the translational transformation from A to B. Both the R matrix and the o vectors are formulated with respect to reference frame A. Since the arm is designed with planar mechanisms, the translational and rotational transformation occur in a single plane. A series of transformations describing the total configuration from the base to the end effector by:

$$H_E^A = H_B^A H_C^B H_D^C H_E^D \tag{6.3}$$

where the result of this calculation is a matrix describing the final position of the position of reference frame E with respect to frame A.

When a module is in the (0) state, a kinematic model based on the Jones kinematic model is used to describe the shape of the soft modules. It is assumed that rotation of the soft modules follows the path of a simple arc with a constant curvature [37-39]. The transformation matrix used for the (0) state is:

$$\mathrm{H}_{(0)} = \begin{bmatrix} \cos(\psi) & -\sin(\psi)\cos(\varphi) & \sin(\psi)\sin(\varphi) & -\kappa^{-1}(\sin(\psi)(1-\cos(\varphi))) \\ \sin(\psi) & \cos(\psi)\cos(\varphi) & -\cos(\psi)\sin(\varphi) & -\kappa^{-1}(\cos(\psi)(1-\cos(\varphi))) \\ 0 & \sin(\varphi) & \cos(\varphi) & \kappa^{-1}\sin(\varphi) \\ 0 & 0 & 0 & 1 \end{bmatrix} \tag{6.4}$$

where $H_{(0)}$ is the transformation matrix for a compressed (0) state module, κ is the curvature, ψ is the angle of curvature, and φ will be zero because there is only arm motion in a single plane. It is assumed during the experiment that there is not out of plane motion, so this zero φ will simplify the (0) state transformation matrix. Also, the planar translation of the actuator frames can be represented by a modified fourth column that describes the translational movement with a relationship of the curvature and rotation angle.

The modified (0) transformation matrix is:

$$\mathrm{H}_{(0)} = \begin{bmatrix} \cos(\psi) & -\sin(\psi) & 0 & -\kappa^{-1}\sin(\psi) \\ \sin(\psi) & \cos(\psi) & 0 & -\kappa^{-1}\cos(\psi) \\ 0 & 0 & 1 & 0 \\ 0 & 0 & 0 & 1 \end{bmatrix} \tag{6.5}$$

The curvature of the rotation is calculated using:

$$\kappa = \frac{1}{r} \tag{6.6}$$

where *r* is the constant radius of the curve, 31.38mm. For an actuator module in the (1) state, it is assumed that the link will not rotate, and the corresponding matrix will represent the transformation:

$$H_{(1)} = \begin{bmatrix} 1 & 0 & 0 & 0 \\ 0 & 1 & 0 & L_{(1)} \\ 0 & 0 & 1 & 0 \\ 0 & 0 & 0 & 1 \end{bmatrix} \tag{6.7}$$

where $H_{(1)}$ is the transformation matrix for a module in the (1) state and $L_{(1)}$ is the extended resting length of the module, 51.83mm.

Results

Overall, the kinematic model agrees with the deformations of the robotic arm. Figure 6.3 displays the seven rotated configurations and the predicted kinematic model. Configurations with one compressed module experienced a 10mm tendon change, configurations with two compressed modules experienced a 20mm tendon change, and the configuration with three compressed modules experienced a 30mm tendon change.

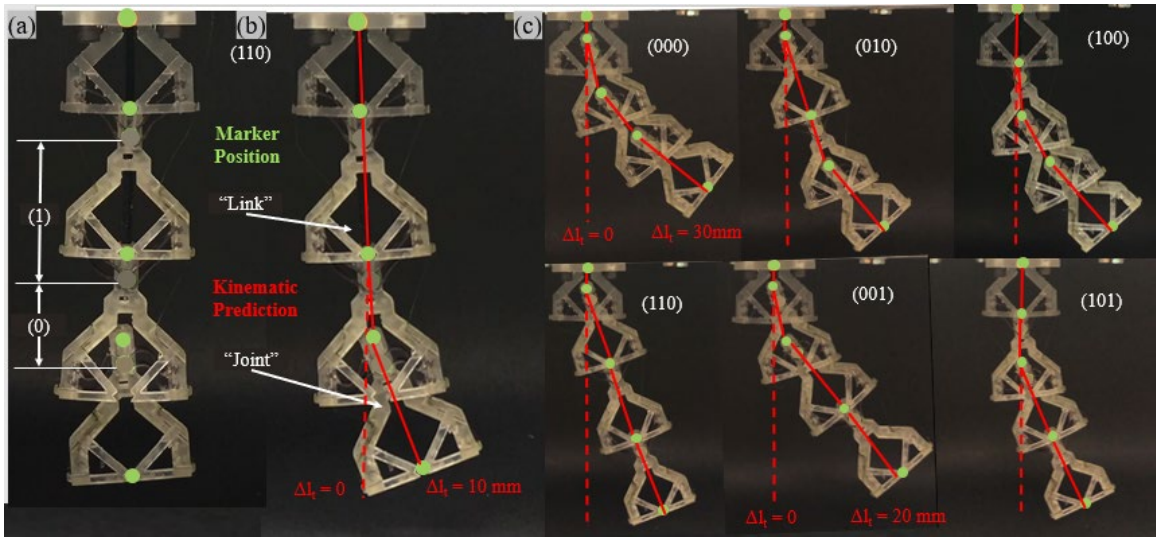

Figure 6.3: Proof of concept test for the compliant locking robotic arm with reconfigurable articulation. a) The initial resting position of the 110 configuration. b) The rotated 110 configuration, where the tendon length was changed by 10mm. Green markers are used for length measurements and red lines show the predicted kinematic model. c) Similar transformation images showing the rotated configuration and the results of the theoretical kinematic model.

Figure 6.4 displays the error analysis of the predicted kinematic model and the actual experimental data. All the error for markers A through D, except for the D marker for 100, had errors of less than 5mm. When compared to the fully extended length of the robotic arm, 187.01mm, that is a 2.7% error. When compared to the fully compressed length of the robotic arm, 126.01mm, that is a 4.0% error. Each of the configurations follows an increasing error trend: as the distance from the origin increases, the error will increase. Each of the different tendon length changes had a configuration with an error exceeding 10mm. The maximum error occurred at the E marker for the 101 configurations, 11.98mm. When compared to the fully extended length, this is a 6.4%

error and compared to the fully compressed length, this is a 9.5% error. All the markers for the zero-load configuration were within 10% error of the total compressed robotic arm length.

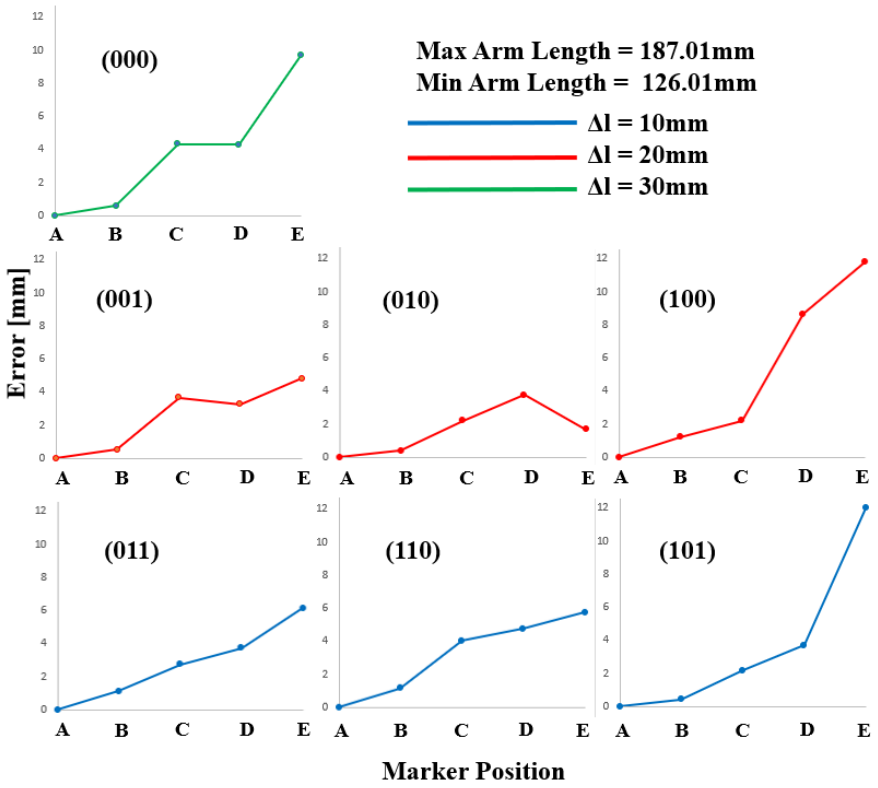

Figure 6.4: Position error for each of the marked position in for the seven configurations. Blue lines show the error for configurations with a single compressed module, red lines show the error for configurations with two compressed modules, and the green line shows the error for the configuration with three compressed modules.

Loading Test

The compliant mechanism robotic arm provides a method of moving an end effector to a user's desired location. Many end effectors exist in the robotics market,

which makes it necessary to test the weight capacity of the robotic arm. The robotic arm should be able to move an end effector with varying loads like unloaded position predictions. The loading test is meant to show that the compliant robotic arm can carry varying loads without compromising predicted kinematic values. The test will also be used to test the loading limits of the three-module robotic arm.

Setup

The robotic arm is setup in the same as the configurations test. The 011 configuration was examined in this test because each marker position was predicted with less than 5% length error maximum load capability will be determined for the minimum change in tendon length. The accuracy from the configuration test will help judge the capability of handling varying load. Figure 6.5 displays the load testing setup. The load was increased by adding small weight to an elastic balloon. The balloon was attached to the end of the robotic arm, marker E, to mimic an end effector with a load.

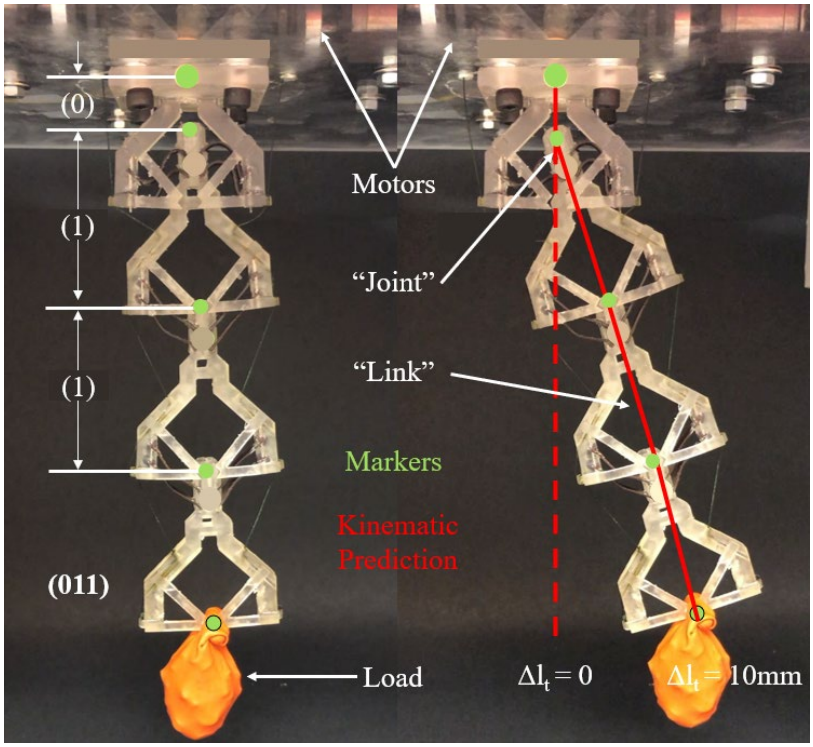

Figure 6.5 Experimental setup for the load testing

Methods

To rotate the 011 configuration to the right, the right tendon was shortened 10mm and the left tendon was lengthened 10mm, according to equation 6.1. The kinematic predictions were calculated using the coordinate transformations in equation 6.3. High resolution pictures were taken during the rotation of the robotic arm to capture each of the position markers. The experimental results were measured using the same process as the configurations test. The test started with a load that was the same weight as the robotic arm, 19.5g. The load increased by a factor of the robotic arms own weight. After

these results were collected, the weight was increased until to find the maximum load until failure.

Results

The robotic arm was able to safely articulate with a load that was ten times its own weight. Figure 6.6 displays the position error analysis as the end loads on the robotic arm increased. When the load factor was below three, the arm visibly rotated with the ease it exhibited without a load. Once the load factor exceeded 3, there was a visible disturbance as the arm rotated into position. Despite the decline smooth rotation, the robotic arm was able to transfer increasing loads with varying accuracies. After the load factor reached five, the E marker experienced an error range of over 10mm. The D marker experienced an error range of 5.0mm, the C marker experienced an error range of 1.1mm and the B marker experienced an error range of 1.2mm. With the increasing variance in the E marker, it was time to test the maximum load capacity of the arm. The load was increased until the arm had visible trouble lifting the load to the correct position. When the load factor reached ten, the test concluded, and the arm could not lift larger loads without the failure.

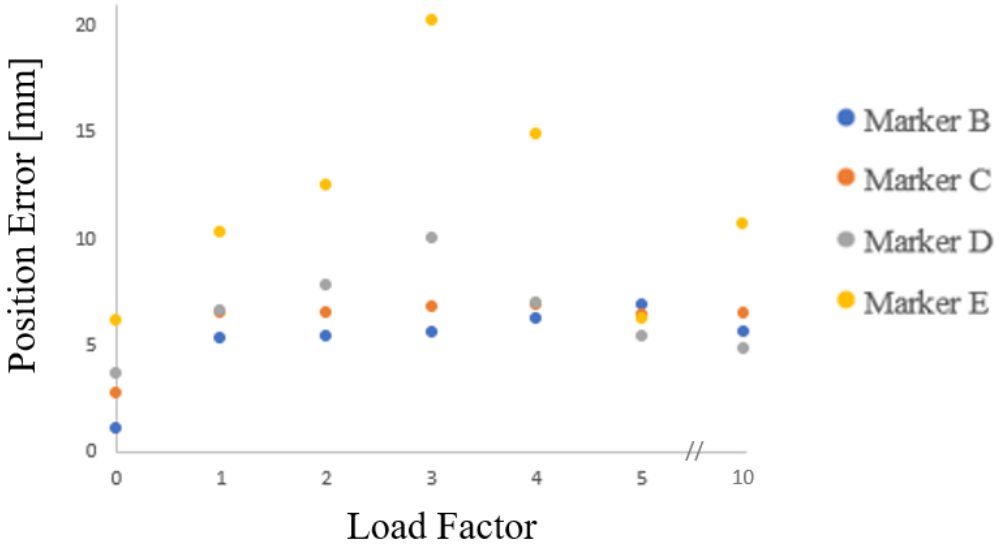

Figure 6.6: Error analysis of the loading test

The loading error was compared to the unloaded condition by finding the error ratio. Marker B had a maximum error that was 6.2 times the unloaded error. Marker C had a maximum error that was 2.5 times the unloaded error. Marker D had a maximum error of 2.7 times the unloaded error. Marker E had a maximum error that was 3.2 times the unloaded error. Overall, the robotic arm could move an end load that was ten times its own weight to an end predicted value with an error of 10.4mm. That is a 5.3% of the fully extended arm length and 8.3% of the fully compressed arm length. When the load factor was 3, the E marker experienced large amount of error. While reviewing the rotation videos for each configuration, it was realized that the 3-load factor test had slack in the right tendon line. The tendons were tight for each of the other rotation test, but a small amount of slack decrease the angle of rotation in the 3-load factor test. So, this

error is end user error because after the 2-load factor test, the actuator arm and tendons were not properly reset and checked before proceeding to the next load factor.

Discussion

A major problem in the field of soft robotics is modeling and controlling a system that continually adapts to its environment. It is necessary to simplify the control methods of a soft robotic manipulator without risking mechanical performance. The compliant locking robotic arm proved its capability of predicting the deformations of the arm with a kinematic model. The discrepancies between the experimental results and theoretical results could derive from fabrication defects, gravity, and other small actuator deformations due to the compliant nature. Test conducted on the robotic arm did not utilize any feedback control. The Arduino took a change in tendon length value and rotated the arm to its desired location. With a feedback system, the arm would be able to adjust the change in tendon length to maintain a more precise end location [40].

CHAPTER SEVEN

CONCLUSION

This study plans a new compliant locking mechanism design that utilizes bistability to achieve stiffness tuning used articulate a robotic arm into unique configurations. The degrees of freedom of the manipulator were reduced by switching the actuator module between a stiff, link-like stable state (1), and a soft, joint like stable state (0). A bending stiffness ratio of 6.4 was achieved and helped reduce the control requirements by introducing bistability. The actuator module produced a stroke length of 20.5mm, which increased the range of motion for the deployable structure. An integrated locking mechanism was designed into the frame. The geometry of the structure allowed the mechanism to unlock from the extended stable state under the natural deflection of the frame arms. In the extended (1) stable position, the actuator can withstand a compressive force almost 100 times its own weight. End users can use the modular design to serially connect the actuator modules to form a robotic arm.

A proof-of-concept robotic arm was constructed from three actuator modules that were tendon-driven. The robotic arm successfully validated the reconfigurable concept through a spine-controlled process that reconfigured the arm modules into different stable states. The motor-controlled tendons allowed the arm to rotate in a single plane for all seven of the configurations. A kinematic model predicted the movements for five critical points along the arm, including the end position. End positions for the seven

configurations were calculated and predicted by controlling that changing length of the tendons. Finally, the robotic arm was able to displace loads up to ten times its own weight, while agreeing with the kinematic model. This shows that the compliant locking robotic arm concept is feasible for soft robotic applications and can manipulate an end effector with a load accurately.

Future Work

There are two ways to advance the future of this study: automating the spine manipulation process and developing a 3D prototype and kinematic model of the robotic arm. Automating the spine further develops the control process of the robotic arm. By designing a way to manipulate the spine through each of the actuator frame, the robotic arm will become fully automated. Eliminating the necessity of human interaction with the robot will increase the safety and performance of the robotic arm.

A three-dimensional design would allow the arm to deform in the XYZ direction instead of a single XY plane. This would increase the versatility of the robotic arm. Figure 7.1 displays the start of a 3D design that uses similar structural features of the 2D model. The model still has a base that allows the entire frame to connect to another frame through flexural members. The frame consists of three arm and base elements that are evenly arrayed, 120 degrees around a center axis. A three-prong design was chosen to incorporate the DH and Jones kinematic model. Three tendons, like the 3D Kresling robotic arm [1] can be threaded through each arm and manipulated to rotate in a three-

dimensional space. A locking mechanism needs to be integrated into this design to further increase the rigidity of the mechanism. Also, further development in the implementation of a spine is needed to control the extension and compression configuration process.

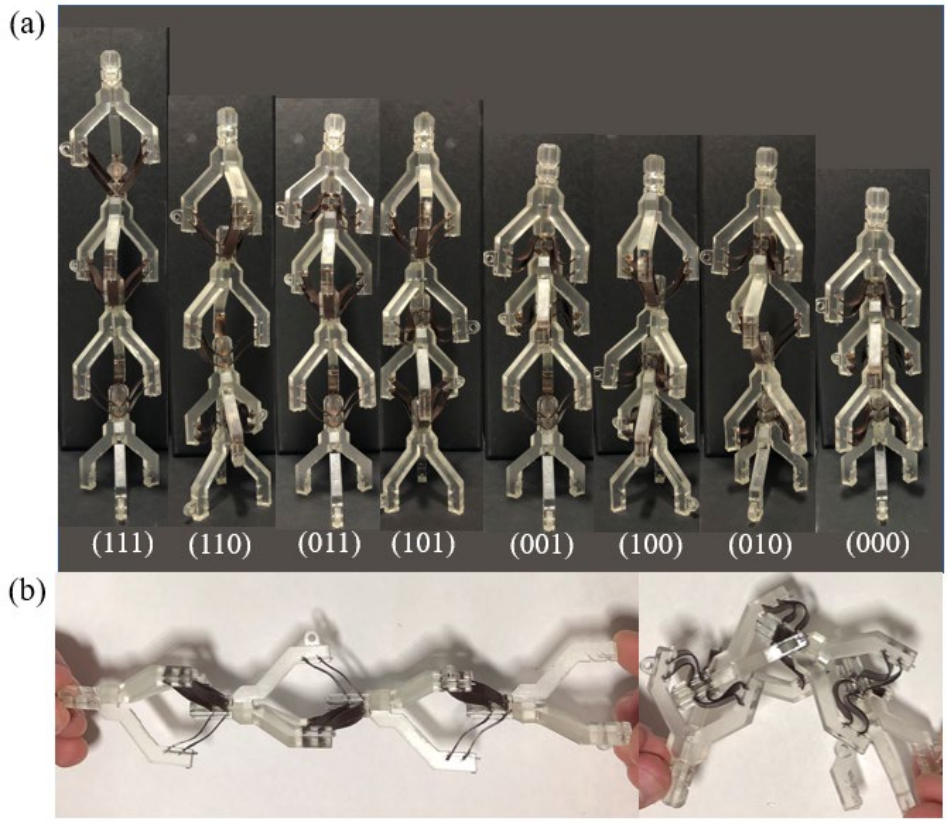

Figure 7.1 The beginning of a 3D compliant actuator design. a) The design exhibits bistability and can be transformed to all 8 configurations. b) The design exhibits a high bending stiffness in the compressed stable position and a lower bending stiffness in the compressed stable position.

APPENDICES

Appendix A

Dimensional Drawings

The critical dimensions for the unit actuator frame are displayed in figure A.1. These dimensions were used throughout the fabrication of the robotic arm. The SLA printing process was able to keep these dimensions very precise during each of the prints.

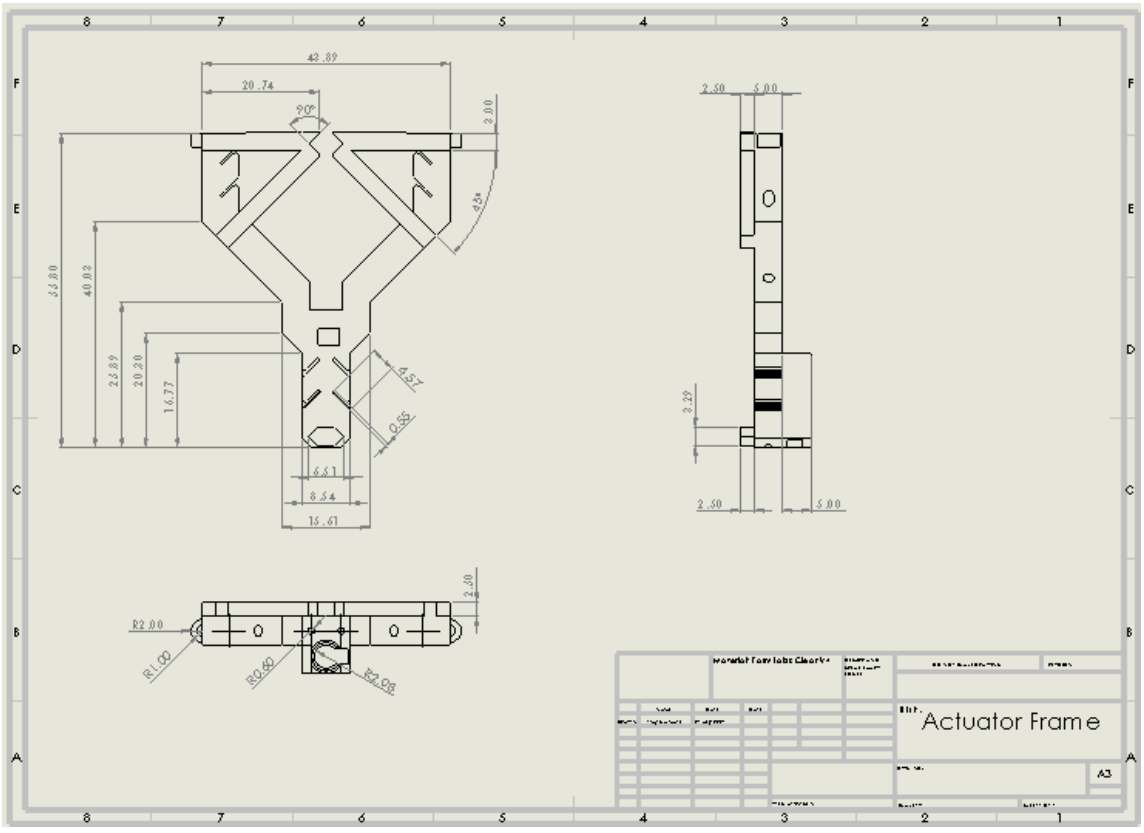

Figure A.1: Frame drawing displaying key dimensions.

The manipulation process of the spine is displayed in figure A.2. This process was performed by the user manipulating the robotic arm into each of the eight configurations.

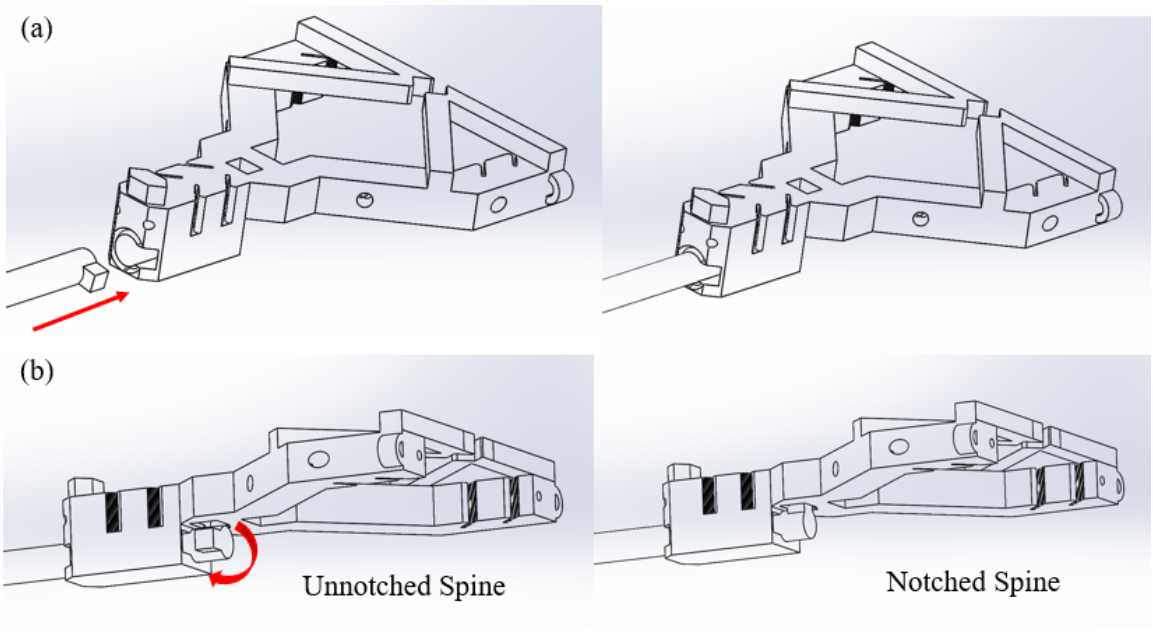

Figure A.2: Manipulation of the spine: a) Align the spine with the spine guide in the frame and push spine through. b) Align the notch with the frame spine notch and rotate the spine 90 degrees to lock the spine tab in the spine notch.

Appendix B

Cantilever Beam Analysis

Figure B.1 displays the problem setup for the cantilever beam analysis. The force on each of the flexural member slots is assumed to be equivalent for all four slots. The actuator frame is symmetric and there are four critical points.

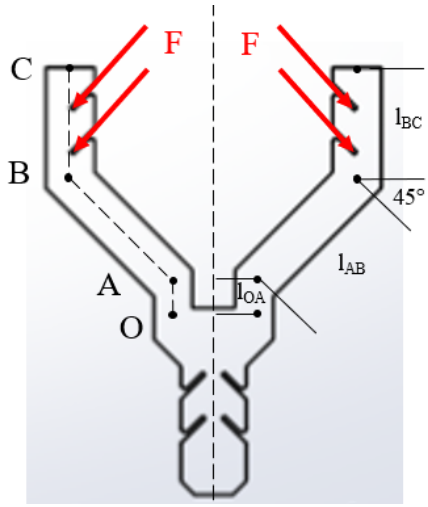

Figure B.1: Cantilever beam analysis diagram

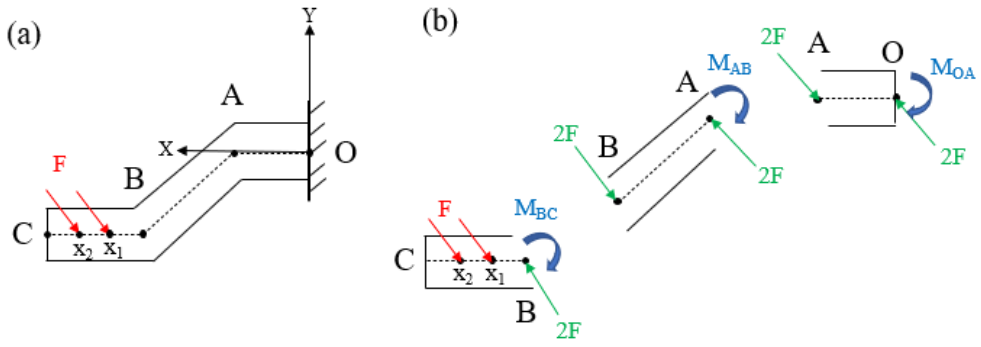

Figure B.2: Decomposition of the cantilever beam frame arm. a) Cantilever beam diagram. b) Decomposed cantilever beam in three sections

Figure B.2 displays the decomposed diagram of the forces and moment for each member of the cantilever beam. Assuming zero net force in the X and Y direction, the moment at point B is equivalent to:

$$\sum M_B = -Fx_1 \sin(45°) - Fx_2 \sin(45°) = -\frac{F\sqrt{2}}{2}(x_1 + x_2) \tag{B.1}$$

where M_B is the moment at point B, F is the force transferred from the flexural members, x_1 is the distance the force acts from point B and x_2 is the distance the force acts from point B. The moment about point A can be calculated using the equation:

$$\sum M_A = -2Fl_{AB} \tag{B.2}$$

where M_A is the moment about point A and l_{AB} is the distance between point A and point B. The moment about point O is calculated using the equation:

$$\sum M_O = -2Fl_{OA} \sin(45°) = -Fl_{OA}\sqrt{2} \tag{B.3}$$

where M_O is the moment about point O and l_{OA} is the distance between point O and A. The deflection of the BC section can be calculated using the equation:

$$\partial_{BC} = \frac{dU_{BC}}{dF} = \frac{1}{EI}\int_0^{l_{BC}} M_B \, x dx \tag{B.4}$$

where δ_{BC} is the deflection of the BC section, E is the Youngs modulus of the frame material, and I is the area moment of inertia of the arm section. The deflection of the AB section was calculated using the equation:

$$\partial_{AB} = \frac{dU_{AB}}{dF} = \frac{1}{EI}\int_0^{l_{AB}} M_A\, x dx \tag{B.5}$$

where δ_{AB} is the deflection of the AB section. The deflection of the OA section was calculated with the equation:

$$\partial_{OA} = \frac{dU_{OA}}{dF} = \frac{1}{EI}\int_0^{l_{OA}} M_O\, x dx \tag{B.6}$$

where δ_{OA} is the deflection of the OA section. The max deflection was calculated by combining all the section deflection:

$$\partial_{max} = \partial_{OA} + \partial_{AB} + \partial_{BC} \tag{B.7}$$

where δ_{max} is the maximum deflection for the frame arm. Each section was then compared to the maximum deflection using the equation:

$$D_i = \frac{\partial_i}{\partial_{max}} \tag{B.8}$$

where D_i is the ratio of the section deflection to the maximum deflection and δ_i is the corresponding deflection of the OA, AB, or BC section. Table B.1 displays the results of the calculation when the dimensions from Appendix A were substituted.

Table B.1 Deflection Ratio Results

D_{OA} [%]	D_{AB} [%]	D_{BC} [%]
0.7	86.7	12.6

Appendix C

Locking Notch Designs and Results

The average unlocking forces for the tested notch designs are displayed in Table C.1. These values were dependent on the geometry of the notch, the geometry of the locking arms, and the location that the locking arms attached to the frame.

Table C.1 Average unlocking values for locking designs

Design	Average Unlocking Force [N]
a	4.48
b	6.45
c	5.69
d	18.41
e	18.43

The locking designed are displayed in picture C.1. Designs d and e were similar, but design was better at resisting moment loads. The notch difference between a-c and e is the width of the notch. Each one still used a 90-degree angle on the inside. The width of the notch could be adjusted to tune the unlocking force.

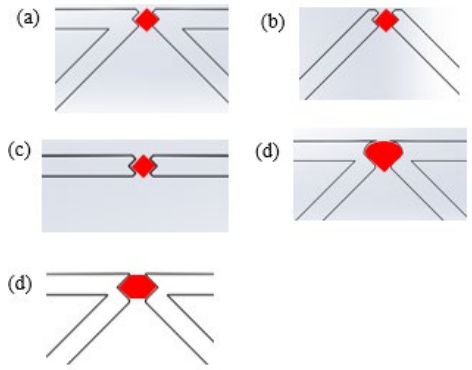

Figure C.1 Five different locking designs

Appendix D

Material Considerations

Table D.1 displays the material properties and the ratios used to make material decisions. Clear resin was chosen for the frame material and HDPE was chosen for the flexural member data. HDPE was available in the sheet thickness that was needed. This material also had a high flexural strength to flexural modulus ratio. Since the frame required less deflection, the strength to Youngs ratio had less of an impact but was still important. Even though clear did not have the highest strength to weight ratio, the material made up for this by having similar modulus values to Polypropylene, which is the recommended frame material for compliant mechanisms.

Table D.1 Material properties and ratio results

Material	S_{ult} [MPa]	E [GPa]	S_{flex} [MPa]	E_{flex} [GPa]	S_{ult}/E	S_{flex}/E_{flex}
PP	79.7	1.46	36.4	1.39	0.055	0.026
HDPE	26.9	0.959	51.9	1.19	0.028	0.044
Clear	38	1.6		1.3	0.024	0
Durable	13	0.24	1	0.04	0.054	0.025
Tough 1500	26	0.94	15	0.44	0.028	0.034
Tough 2000	29	1.2	17	0.45	0.024	0.038
Rigid 4000	33	2.1	43	1.4	0.016	0.031
Rigid 10k	55	7.5	84	6	0.007	0.014

The flexural member thickness was 0.55mm because thicker flexural members experienced plastic deformation during the buckling cycle. Figure D.1 displays the testing results for differing length flexural members after a cycle test. After the testing, it is obvious that the 0.80mm flexural member in figure B.1c experience plastic

deformation at each of the two curve peaks. The flexural member no longer stayed straight when at a relaxed state. The 0.63mm flexural thickness experienced less plastic deformation, but a slight curvature was still permanently shaped into the member after the test. The 0.55mm flexural thickness remained straight after the cycle testing, leaving no signs of plastic deformation. This thickness was chosen because it would allow the actuator to have an increased cycle life.

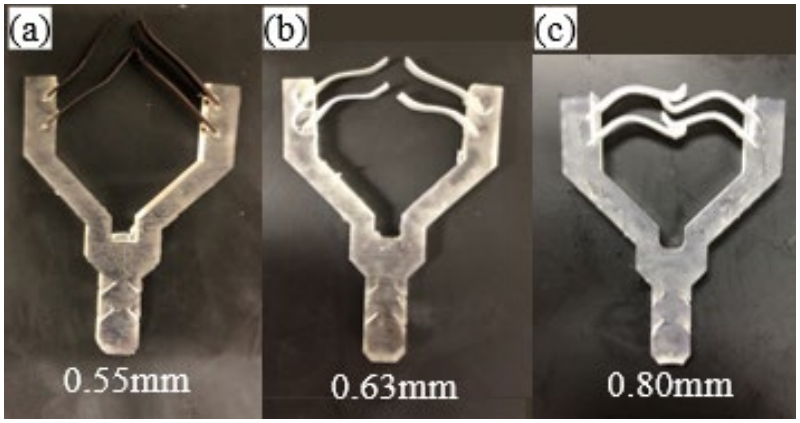

Figure D.1: Flexural member plastic deformation analysis for: a) the 0.55mm, b) the 0.63mm, and c) the 0.80mm.

WORKS CITED

[1] Kaufmann , Joshua, and Suyi Li. 2020. *Harnessing the Multi-Stability of Kresling Origami for Reconfigurable Articulation in Soft Robotic Arms.* Clemson , South Carolina , May 9.

[2] Eder, M., M. Karl, A. Knoll, and S. Riesner. 2014. "*Continuum worm-like robotic mechanism with decentral control architecture*." *2014 IEEE International Conference on Automation Science and Engineering (CASE).* Taipei, Taiwan: IEEE.

[3] Li, Sihui , Raagini Rameshwar, Ann Marie Votta, and Cagdas D. Onal. 2019. "*Intuitive Control of a Robotic Arm and Hand*." *IEEE ROBOTICS AND AUTOMATION LETTERS*

[4] Gundula Runge, Sabrina Zellmer, Tobias Preller, Georg Garnweitner, Annika Raatz, "*Actuation principles for the bioinspired soft robotic manipulator spineman*", *Robotics and Biomimetics (ROBIO) 2015 IEEE International Conference on*, pp. 1329-1336, 2015.

[5] Howell, Larry, Brian Olsen, and S. Magleby. 2013. *Handbook of Compliant Mechanisms* . Provo, UT: BYU.

[6] Sanan, Siddharth, Michael Ornstein, and Christopher Atkeson. 2011. "*Physical human interaction for an inflatable manipulator*." *Annual International Conference of the IEEE Engineering in Medicine and Biology Society.* Boston, MA: IEEE.

[7] Stilli, Agostino, Helge Wurdemann, and Kaspar Althoefer. 2017. "A Novel Concept for Safe, Stiffness-Controllable Robot Links." *Soft Robotics*

[8] Venkiteswaran, Venkatsubramanian Kalpathy. 2017. "*Development of a Design Framework for Compliant Mechanisms using Pseudo-Rigid-Body Models*." *The Ohio State University.*

[9] Iida, Fumiya, and Cecilia Laschi. 2011. "Soft Robotics: Challenges and Perspectives." *Procedia Computer Science* 99-102.

[10] Uozumi, Seiji, S. Shimizu, T. Matsunaga, T. Nakano, and K. Ohnishi. 2015. "*Verification of Twist Drive system and its application to haptic robot hand*." *2015 IEEE International Conference on Industrial Technology (ICIT).* Seville, Spain: IEEE.

[11] Friesen, Jeffrey. 2014. "*Modular Joints for Soft Robotics*." *NASA.* December 4. Accessed July 1, 2021. https://www.nasa.gov/content/modular-joints-for-soft-robots/.

[12] Sumbre, German, Graziano Fiorito, Tamar Flash, and Binyamin Hochner. 2016. *"Octopuses Use a Human-like Strategy to Control Precise Point-to-Point Arm Movements*." April 18. https://www.cell.com/current-biology/fulltext/S0960-9822(06)01274-7?_returnURL=https%3A%2F%2Flinkinghub.elsevier.com%2Fretrieve%2Fpii%2FS0960982206012747%3Fshowall%3Dtrue.

[13] Renda, F., and M. Giorelli. 2014. "*Dynamic Model of a Multibending Soft Robot Arm Driven by Cables*." *IEEE Transactions on Robotics* .

[14] A. D. Marchese, K. Komorowski, C. D. Onal and D. Rus, *"Design and control of a soft and continuously deformable 2D robotic manipulation system*," *2014 IEEE International Conference on Robotics and Automation (ICRA)*, 2014, pp. 2189-2196, doi: 10.1109/ICRA.2014.6907161.

[15] Kim, Yong-Jae, Shanbao Cheng, Sangbae Kim, and Karl Iagnemma. 2013. "*A Novel Layer Jamming Mechanism with Tunable Stiffness Capability for Minimally Invasive Surgery*." *IEEE Transaction on Robotics* 1031-1042.

[16] Cheng, Nadia et al. "*Design and Analysis of a Soft Mobile Robot Composed of Multiple Thermally Activated Joints Driven by a Single Actuator*." IEEE, 2010. 5207–5212. Web. 4 Apr. 2012. ©2010 Institute of Electrical and Electronics Engineers

[17] Ishii, Hiroya, and Kwun-Lon Ting. 2004. "*SMA actuated compliant bistable mechanisms*." *Mechatronics* 421-437

[18] Currie, Neil GR, and Giulia E Fenci. 2017. "*Deployable Structures Classification: A Review*." *International Journal of Space Structures* 1-19.

[19] Zhai, Zirui, Yong Wang, and Hanqing Jiang. 2018. "*Origami-inspired, On-demand Deployable and Collapsible Mechanical Metamaterials with Tunable Stiffness* ." *Proceedings of the National Academy of Sciences of the United States of America* 1-6.

[20] Robinson, Jacob Marc. 2015. "*A Compliant Mechanism-Based Variable-Stiffness Joint*." BYU Scholar sArchive , April 1.

[21] Koli, Ashish B., "*A generalized approach for compliant mechanism design using the synthesis with compliance method, with experimental validation*" (2013). Masters Theses. 7099.

https://scholarsmine.mst.edu/masters_theses/7099Large-Displacement Linear-Motion Compliant Mechanisms

[22] Choi H S, Ding J L, Bandyopadhyay A, Anderson M J and Bose S 2008 *Characterization and modeling of a piezoelectric micromachined ultrasonic transducer with a very large length/width aspect ratio* J. Micromech. Microeng. 18 25037

[23] Anderson, Jeffrey K., "Piezoresistive Sensing of Bistable Micro Mechanism State" (2005). Theses and Dissertations. 692. https://scholarsarchive.byu.edu/etd/692

[24] Holst, Gregory, Gregory Teichert, and Brian Jensen. 2011. "*Modeling and Experiments of Buckling Modes and Deflection of Fixed-Guided Beams in Compliant Mechanisms.*" *Journal of Mechanical Design.*

[25] Shigley, Joseph Edward. *Standard Handbook of Machine Design*. Knovel, 2006.

[26] Ma, Fulei, Guimin Chen, and Guangbo Hao. 2018. "Mechanical Sciences." *Determining the Range of Allowable Axial Force for the Third-Order Beam Constraint Model.* Copernicus Publications , January 22.

[27] n.d. *Consideration of Slenderness Effect in Columns.* Memphis, TN.

[28] Rosato, Dominick, and Donald Rosato. 2003. "*Plastic Engineered Product Design*." New York, NY: Elsevier.

[29] Zhao, Jian, Jianyuan Jia, Xiaoping He, and Hongxi Wang. 2008. "*Post-buckling and Snap-Through Behavior of Inclined Slender Beams.*" *Journal of Applied Mechanics.*

[30] Chen, T., Mueller, J. & Shea, K. Integrated Design and Simulation of Tunable, Multi-State Structures Fabricated Monolithically with Multi-Material 3D Printing. *Sci Rep* **7,** 45671 (2017). https://doi.org/10.1038/srep45671

[31] Korsunsky, Alexander. 2017. "Chapter 2 - *Elastic and Inelastic Deformation and Residual Stress.*" In *A Teaching Essay on Residual Stresses and Eigenstrains*, by Alexander Korsunsky, 5-20. Oxford.

[32] "Material Library: *Advanced Materials Designed to Deliver Beautiful Results.*" *Formlabs.* April 18. https://sourcegraphics.com/files/8315/4119/7144/MaterialsBooklet-SG.pdf.Material

[33] 2021. *formlabs: Material Library.* Accessed July 1, 2021. https://formlabs-media.formlabs.com/datasheets/1901266-TDS-ENUS-0.pdf.

[34] Ahmed Hassan Awad, Ramadan El Gamasy, Ayman Abd El Wahab, Mohamed Hazem Abdellatif, *Mechanical and Physical Properties of PP and HDPE*, *Engineering Science*. Vol. 4, No. 2, 2019, pp. 34-42. doi: 10.11648/j.es.20190402.12

[35] Merriam, Ezekiel G., "*Stiffness Reduction Strategies for Additively Manufactured Compliant Mechanisms*" (2016). Theses and Dissertations. 5873. https://scholarsarchive.byu.edu/etd/5873

[36] Kuchenbecker, Katherine. 2012. "*Denavit-Hartenberg (DH).*"Philadelphia, PA, September 20

[37] Chawla, Anant, Chase G. Frazelle and I. Walker. "*A Comparison of Constant Curvature Forward Kinematics for Multisection Continuum Manipulators.*" *2018 Second IEEE International Conference on Robotic Computing (IRC)* (2018): 217-223.

[38] B. A. Jones and I. D. Walker. 2006. "*Kinematics for multisection continuum robots*." Trans. Rob. 22, 1 (November 2006), 43–55. DOI:https://doi.org/10.1109/TRO.2005.861458

[39] D. B. Camarillo, C. F. Milne, C. R. Carlson, M. R. Zinn, and J. K. Salisbury. 2008. "*Mechanics Modeling of Tendon-Driven Continuum Manipulators"*. Trans. Rob. 24, 6 (December 2008), 1262–1273. DOI:https://doi.org/10.1109/TRO.2008.2002311

[40] George Thuruthel, T., Ansari, Y., Falotico, E., & Laschi, C. (2018). "C*ontrol Strategies for Soft Robotic Manipulators: A Survey. Soft robotics,"5*(2), 149–163. https://doi.org/10.1089/soro.2017.0007